Chapter 4

Theory of Fiber Bragg Gratings

Wave propagation in optical fibers is analyzed by solving Maxwell's equations with appropriate boundary conditions. The problem of finding solutions to the wave-propagation equations is simplified by assuming weak guidance, which allows the decomposition of the modes into an orthogonal set of transversely polarized modes [1–3]. The solutions provide the basic field distributions of the bound and radiation modes of the waveguide. These modes propagate without coupling in the absence of any perturbation (e.g., bend). Coupling of specific propagating modes can occur if the waveguide has a phase and/or amplitude perturbation that is periodic with a perturbation "phase/amplitude-constant" close to the sum or difference between the propagation constants of the modes. The technique normally applied for solving this type of a problem is coupled-mode theory [4–9]. The method assumes that the mode fields of the unperturbed waveguide remain unchanged in the presence of weak perturbation. This approach provides a set of first-order differential equations for the change in the amplitude of the fields along the fiber, which have analytical solutions for uniform sinusoidal periodic perturbations.

A fiber Bragg grating of a constant refractive index modulation and period therefore has an analytical solution. A complex grating may be considered to be a concatenation of several small sections, each of constant period and unique refractive index modulation. Thus, the modeling of the transfer characteristics of fiber Bragg gratings becomes a relatively simple

matter, and the application of the transfer matrix method [10] provides a clear and fast technique for analyzing more complex structures.

Another technique for solving the transfer function of fiber Bragg gratings is by the application of a scheme proposed by Rouard [11] for a multilayer dielectric thin film and applied by Weller-Brophy and Hall [12,13]. The method relies on the calculation of the reflected and transmitted fields at an interface between two dielectric slabs of dissimilar refractive indexes. Its equivalent reflectivity and phase then replace the slab. Using a matrix method, the reflection and phase response of a single period may be evaluated. Alternatively, using the analytical solution of a grating with a uniform period and refractive index modulation as in the previous method, the field reflection and transmission coefficients of a *single period* may be used instead. However, the thin-film approach does allow a refractive index modulation of arbitrary shape (not necessarily sinusoidal, but triangular or other) to be modeled with ease and can handle effects of saturation of the refractive index modulation. The disadvantage of Rouard's technique is the long computation time and the limited dynamic range owing to rounding errors.

The Bloch theory [14,15] approach, which results in the exact eigenmode solutions of periodic structures, has been used to analyze complex gratings [16] as well. This approach can lead to a deeper physical insight into the dispersion characteristics of gratings. A more recent approach taken by Peral *et al.* [17] has been to develop the Gel'Fand–Levitan–Marchenko coupled integral equations [18] to exactly solve the inverse scattering problem for the design of a desired filter. Peral *et al.* have combined the attributes of the Fourier transform technique [19,20] (useful for low reflection coefficients, since it does not take account of resonance effects within the grating), the local reflection method [21], and optimization of the inverse scattering problem [22,23] to present a new method that allows the design of gratings with required features in both phase and reflection. The method has been recently applied to fabricate near "top-hat" reflectivity filters with low dispersion [24]. Other theoretical tools such as the effective index method [25], useful for planar waveguide applications, discrete-time [26], Hamiltonian [27], and variational [28], are recommended to the interested reader. For nonlinear gratings, the generalized matrix approach [29] has also been used. For ultrastrong gratings, the matrix method can be modified to avoid the problems of the slowly varying approximation [30].

The straightforward transfer matrix method provides high accuracy for modeling in the frequency domain. Many representative varieties of the types and physical forms of practically realizable gratings may be analyzed in this way.

4.1 Wave Propagation

The theory of fiber Bragg gratings may be developed by considering the propagation of modes in an optical fiber. Although guided wave optics is well established, the relationship between the mode and the refractive index perturbation in a Bragg grating plays an important role on the overall efficiency and type of scattering allowed by the symmetry of the problem. Here, wave-propagation in optical fiber is introduced, followed by the theory of mode coupling.

We begin with the constitutive relations

$$\overline{D} = \varepsilon_0 \overline{E} + \overline{P} \tag{4.1.1}$$

$$\overline{B} = \mu_0 \overline{H} \tag{4.1.2}$$

where ε_0 is the dielectric constant and μ_0 is the magnetic permeability, both scalar quantities; $\overline{D}$ is the electric displacement vector; $\overline{E}$ is the applied electric; $\overline{B}$ and $\overline{H}$ are the magnetic flux and field vectors, respectively; and $\overline{P}$ is the induced polarization,

$$\overline{P} = \varepsilon_0 \chi_{ij}^{(1)} \overline{E}. \tag{4.1.3}$$

The linear susceptibility $\chi_{ij}^{(1)}$ is in general a second-rank tensor with two laboratory frame polarization subscripts ij and is related to the permittivity tensor ε_{ij} with similar subscripts as

$$\varepsilon_{ij} = 1 + \chi_{ij}^{(1)}. \tag{4.1.4}$$

Assuming that the dielectric waveguide is source free, so that

$$\nabla \cdot \overline{D} = 0, \tag{4.1.5}$$

and in the absence of ferromagnetic materials,

$$\nabla \cdot \overline{B} = 0, \tag{4.1.6}$$

the electric field described in complex notation is

$$\overline{E} = \frac{1}{2}[Ee^{i(\omega t - \beta z)} + Ee^{-i(\omega t - \beta z)}], \tag{4.1.7}$$

and the induced polarization vector is also similarly defined.

Using Maxwell's equations,

$$\nabla \times \overline{E} = -\frac{\partial \overline{B}}{\partial t} \tag{4.1.8}$$

$$\nabla \times \overline{H} = \frac{\partial \overline{D}}{\partial t} + \overline{J}, \tag{4.1.9}$$

where J is the displacement current, and using Eq. (4.1.1) in Eq. (4.1.9) and with $J = 0$, we get

$$\nabla \times \overline{H} = \frac{\partial}{\partial t}[\varepsilon_0 \overline{E} + \overline{P}]. \tag{4.1.10}$$

Taking the curl of Eq. (4.1.8) and using Eqs. (4.1.2)–(4.1.5) and the time derivative of Eq. (4.1.10), the wave equation is easily shown to be

$$\nabla^2 \overline{E} = \mu_0 \varepsilon_0 \frac{\partial^2 \overline{E}}{\partial t^2} + \mu_0 \frac{\partial^2 \overline{P}}{\partial t^2}. \tag{4.1.11}$$

Using Eq. (4.1.3) and (4.1.4) in (4.1.11), we arrive at

$$\nabla^2 \overline{E} = \mu_0 \varepsilon_0 \frac{\partial^2}{\partial t^2}[1 + \chi_{ij}^{(1)}]\overline{E}, \tag{4.1.12}$$

or

$$\nabla^2 \overline{E} = \mu_0 \varepsilon_0 \varepsilon_{ij} \frac{\partial^2 \overline{E}}{\partial t^2}. \tag{4.1.13}$$

4.1.1 Waveguides

The next step in the analysis is to introduce guided modes of the optical fiber into the wave equation. The modes of an optical fiber can be described as a summation of l transverse guided mode amplitudes, $A_\mu(z)$, along with a continuum of radiation modes, $A_\rho(z)$ [2], with corresponding propagation constant, $\beta\mu$ and $\beta\rho$,

$$E_t = \frac{1}{2}\sum_{\mu=1}^{\mu=1}[A_\mu(z)\xi_{\mu t}e^{i(\omega t - \beta_\mu z)} + cc] + \sum \int_{\rho=0}^{\rho=\infty} A_\rho(z)\xi_{\rho t}e^{i(\omega t - \beta_\rho z)}\, d\rho, \tag{4.1.14}$$

where $\xi_{\mu t}$ and $\xi_{\rho t}$ are the radial transverse field distributions of the μth guided and ρth radiation modes, respectively. Here the polarization of the fields has been implicitly included in the transverse subscript, t. The summation before the integral in Eq. (4.1.14) is a reminder that all the different types of radiation modes must also be accounted for [e.g., transverse electric (TE) and transverse magnetic (TM), as well as the hybrid (EH and HE) modes]. The following orthogonality relationship ensures that the power carried in the μth mode in watts is $|A_{\mu t}|^2$:

$$1/2 \int_{-\infty}^{+\infty} \int_{-\infty}^{+\infty} \hat{e}_z \cdot [\xi_{\mu t} \times \xi_{vt}^*] dxdy = 1/2 \left[\frac{\beta\mu}{\omega\mu_0} \right] \int_{-\infty}^{+\infty} \int_{-\infty}^{+\infty} \xi_{\mu t} \cdot \xi_{vt}^* dxdy = \delta_{\mu v}. \tag{4.1.15}$$

Here, $\hat{e}_z$ is a unit vector along the propagation direction z. $\delta_{\mu v}$ is Kronecker's delta and is unity for $\mu = v$, but zero otherwise. Note that this result is identical to integrating Poynting's vector (power-flow density) for the mode field transversely across the waveguide. In the case of radiation modes, $\delta_{\mu v}$ is the Dirac delta function which is infinite for $\mu = v$ and zero for $\mu \neq v$. Equation (4.1.15) applies to the weakly guiding case for which the longitudinal component of the electric field is much smaller than the transverse component, rendering the modes predominantly linearly polarized in the transverse direction to the direction of propagation [1]. Hence, the transverse component of the magnetic field is

$$H_t = \sqrt{\frac{\varepsilon_0 \varepsilon_r}{\mu_0}} \left[\hat{e}_z \frac{\partial}{\partial z} \times \xi_t \right]. \tag{4.1.16}$$

The fields satisfy the wave equation (4.1.13) as well as being bounded by the waveguide. The mode fields in the core are J-Bessel functions and K-Bessel functions in the cladding of a cylindrical waveguide. In the general case, the solutions are two sets of orthogonally polarized modes. The transverse fields for the μth x-polarized mode that satisfy the wave equation (4.1.13) are then given by [2]

$$\xi_x = C_\mu J_\mu \left(u \frac{r}{a} \right) \begin{Bmatrix} \cos \mu\phi \\ \sin \mu\phi \end{Bmatrix} \tag{4.1.17}$$

$$H_y = n_{eff} \sqrt{\frac{\varepsilon_0}{\mu_0}} \xi_x, \tag{4.1.18}$$

and the corresponding fields in the cladding are

$$\xi_x = C_\mu \frac{J_\mu(u)}{K_\mu(w)} K_\mu\left(w \frac{r}{a}\right)\begin{Bmatrix}\cos \mu\phi \\ \sin \mu\phi\end{Bmatrix} \tag{4.1.19}$$

$$H_y = n_{eff}\sqrt{\frac{\varepsilon_0}{\mu_0}}\,\xi_x, \tag{4.1.20}$$

where the following normalized parameters have been used in Eqs. (4.1.17)–(4.1.20):

$$v = \frac{2\pi a}{\lambda}\sqrt{n_{core}^2 - n_{clad}^2} \tag{4.1.21}$$

$$u = \frac{2\pi a}{\lambda}\sqrt{n_{core}^2 - n_{eff}^2} \tag{4.1.22}$$

$$w^2 = v^2 - u^2, \tag{4.1.23}$$

and

$$n_{eff} = n_{clad}\left[b\left(\frac{n_{core} - n_{clad}}{n_{clad}}\right) + 1\right], \tag{4.1.24}$$

where n_{eff} is the effective index of the mode and

$$b = \frac{w^2}{u^2}. \tag{4.1.25}$$

Finally, assuming only a single polarization, the y-polarized mode,

$$\xi_y = H_x = 0. \tag{4.1.26}$$

The choice of the cosine or the sine term for the modes is somewhat arbitrary for perfectly circular nonbirefringent fibers. These sets of modes become degenerate. Since the power carried in the mode in watts is $|A_\mu|^2$, from the Poynting's vector relationship of Eq. (4.1.15), the normalization constant C_μ can be expressed as

$$C_\mu = \frac{2w}{av}\left[\frac{\sqrt{\mu_0/\varepsilon_0}}{n_{eff}\,\pi\varepsilon_\mu |J_{\mu-1}(u)J_{\mu+1}(u)|}\right]^{1/2}, \tag{4.1.27}$$

where $e_\mu = 2$ when $\mu = 0$ (fundamental mode) and 1 for $\mu \neq 0$. Matching the fields at the core–cladding boundary results in the waveguide characteristic eigenvalue equation, which may be solved to calculate the propagation constants of the modes:

$$u \frac{J_{\mu\pm1}(u)}{J_\mu(u)} = w \frac{K_{\mu\pm1}(w)}{K_\mu(w)}. \tag{4.1.28}$$

4.2 Coupled-mode theory

The waveguide modes satisfy the unperturbed wave equation (4.1.13) and have solutions described in Eqs. (4.1.17) through (4.1.20). In order to derive the coupled mode equations, effects of perturbation have to be included, assuming that the modes of the unperturbed waveguide remain unchanged. We begin with the wave equation (4.1.11)

$$\nabla^2 \overline{E} = \mu_0 \varepsilon_0 \frac{\partial^2 \overline{E}}{\partial t^2} + \mu_0 \frac{\partial^2 \overline{P}}{\partial t^2}. \tag{4.2.1}$$

Assuming that wave propagation takes place in a perturbed system with a dielectric grating, the total polarization response of the dielectric medium described in Eq. (4.2.1) can be separated into two terms, unperturbed and the perturbed polarization, as

$$\overline{P} = \overline{P}_{unpert} + \overline{P}_{grating}, \tag{4.2.2}$$

where

$$\overline{P}_{unpert} = \varepsilon_0 \chi^{(1)} \overline{E}_\mu. \tag{4.2.3}$$

Equation (4.2.1) thus becomes,

$$\nabla^2 E_{\mu t} = \mu_0 \varepsilon_0 \varepsilon_r \frac{\partial^2}{\partial t^2} E_{\mu t} + \mu_0 \frac{\partial^2}{\partial t^2} P_{grating,\mu}, \tag{4.2.4}$$

where the subscripts refer to the transverse mode number μ. For the present, the nature of the perturbed polarization, which is driven by the propagating electric field and is due to the presence of the grating, is a detail which will be included later.

Substituting the modes in Eq. (4.1.14) into (4.2.4) provides the following relationship:

$$\nabla^2\left[\frac{1}{2}\sum_{\mu=1}^{\mu=l}[A_\mu(z)\xi_{\mu t}e^{i(\omega t-\beta_\mu z)}+cc]+\sum\int_{\rho=0}^{\rho=\infty}A_\rho(z)\xi_{\rho t}e^{i(\omega t-\beta_\rho z)}\,d\rho\right]$$

$$-\mu_0\varepsilon_0\varepsilon_r\frac{\partial^2}{\partial t^2}\left[\frac{1}{2}\sum_{\mu=1}^{\mu=1}[A_\mu(z)\xi_{\mu t}e^{i(\omega t-\beta_\mu z)}+cc]+\sum\int_{\rho=0}^{\rho=\infty}A_\rho(z)\xi_{\rho t}e^{i(\omega t-\beta_\rho z)}\,d\rho\right]$$

$$=\mu_0\frac{\partial^2}{\partial t^2}P_{grating,\mu}. \tag{4.2.5}$$

Ignoring coupling to the radiation modes for the moment allows the left-hand side of Eq. (4.1.13) to be expanded. In weak coupling, further simplification is possible by applying the slowly varying envelope approximation (SVEA). This requires that the amplitude of the mode change slowly over a distance of the wavelength of the light as

$$\frac{\partial^2 A_\mu}{\partial z^2}\ll\beta_\mu\frac{\partial A_\mu}{\partial z}, \tag{4.2.6}$$

so that

$$\nabla^2E_t=\frac{1}{2}\sum_{\mu=1}^{\mu=1}\left[-2i\beta_\mu\frac{\partial A_\mu}{\partial z}\xi_{\mu t}e^{i(\omega t-\beta_\mu z)}-\beta_\mu^2A_\mu\xi_{\mu t}e^{i(\omega t-\beta_\mu z)}+cc\right]. \tag{4.2.7}$$

Expanding the second term in Eq. (4.2.5), noting that $\omega^2\mu_0\varepsilon_0\varepsilon_r=\beta_\mu^2$, and combining with Eq. (4.2.7), the wave equation simplifies to

$$\sum_{\mu=1}^{\mu=l}\left[-i\beta_\mu\frac{\partial A_\mu}{\partial z}\xi_{\mu t}e^{i(\omega t-\beta_\mu z)}+cc\right]=\mu_0\frac{\partial^2}{\partial t^2}P_{grating,t}. \tag{4.2.8}$$

Here, the subscript t on the polarization $P_{grating,t}$ reminds us that the grating has a transverse profile. Multiplying both sides of Eq. (4.2.8) by ξ_μ^* and integrating over the wave-guide cross-section leads to

$$\sum_{\mu=1}^{\mu=1}\int_{-\infty}^{+\infty}\int_{-\infty}^{+\infty}\left[-i\beta_\mu\frac{\partial A_\mu}{\partial z}\xi_{\mu t}\xi_{\mu t}^*e^{i(\omega t-\beta_\mu z)}+cc\right]dxdy$$

$$=\int_{-\infty}^{+\infty}\int_{-\infty}^{+\infty}\mu_0\frac{\partial^2}{\partial t^2}P_{grating,t}\xi_{\mu t}^*\,dxdy. \tag{4.2.9}$$

Applying the orthogonality relationship of Eq. (4.1.15) directly results in

$$\sum_{\mu=1}^{\mu=l}\left[-2i\omega\mu_0\frac{\partial A_\mu}{\partial z}e^{i(\omega t-\beta_\mu z)}+cc\right] = \int_{-\infty}^{+\infty}\int_{-\infty}^{+\infty}\mu_0\frac{\partial^2}{\partial t^2}P_{grating,t}\xi_{\mu t}^{*}\,dxdy. \tag{4.2.10}$$

Equation (4.2.10) is fundamentally the wave propagation equation, which can be used to describe a variety of phenomena in the coupling of modes. Equation (4.2.10) applies to a set of forward- and backward-propagating modes; it is now easy to see how mode coupling occurs by introducing forward- and backward-propagating modes. The total transverse field may be described as a sum of both fields, not necessarily composed of the same mode order:

$$E_t = \frac{1}{2}\left(A_v\xi_{vt}e^{i(\omega t-\beta_v z)}+cc+B_\mu\xi_{\mu t}e^{i(\omega t+\beta_\mu z)}+cc\right) \tag{4.2.11}$$

$$H_t = \frac{1}{2}\left(A_vH_{vt}e^{i(\omega t-\beta_v z)}+cc-B_\mu H_{\mu t}e^{i(\omega t+\beta_\mu z)}-cc\right). \tag{4.2.12}$$

Here the negative sign in the exponent signifies the forward- and the positive sign the backward-propagating mode, respectively. The modes of a waveguide form an orthogonal set, which in an ideal fiber will not couple unless there is a perturbation. Using Eqs. (4.2.11) and (4.2.12) in Eq. (4.2.10) leads to

$$\left[\frac{\partial A_v}{\partial z}e^{i(\omega t-\beta_v z)}+cc\right]-\left[\frac{\partial B_\mu}{\partial z}e^{i(\omega t+\beta_\mu z)}+cc\right] = +\frac{i}{2\omega}\int_{-\infty}^{+\infty}\int_{-\infty}^{+\infty}\frac{\partial^2}{\partial t^2}P_{grating,t}\xi_{\mu,vt}^{*}\,dxdy \tag{4.2.13}$$

4.2.1 Spatially periodic refractive index modulation

In a medium in which the dielectric constant varies periodically along the wave-propagation direction, the total polarization can be defined with the perturbed permittivity, $\Delta\varepsilon(z)$ and the applied field as

$$P = \varepsilon_0[\varepsilon_r - 1 + \Delta\varepsilon(z)]E_\mu. \tag{4.2.14}$$

The terms within the parentheses are equivalent to $\chi^{(1)}$, and ε_r is the relative permittivity of the unperturbed core. The constitutive relations between the permittivity of a material and the refractive index n result in the perturbation modulation index being derived from $n^2 = \varepsilon_r$ so that

$$[n + \delta n(z)]^2 = \varepsilon_r + \Delta\varepsilon(z). \tag{4.2.15}$$

Assuming the perturbation to be a small fraction of the refractive index, it follows that

$$\Delta\varepsilon(z) \approx 2n\delta n(z). \tag{4.2.16}$$

Defining the refractive index modulation of the grating as

$$\delta n(z) = \overline{\Delta n}\left\{1 + \frac{\nu}{2}\left(e^{i[(2\pi N/\Lambda)z + \phi(z)]} + cc\right)\right\}, \tag{4.2.17}$$

where $\overline{\Delta n}$ is the refractive index change averaged over a single period of the grating, v is the visibility of the fringes, and the exponent term along with the complex conjugate cc describe the real periodic modulation in complex notation. An arbitrary spatially varying phase change of $\phi(z)$ has been included. Λ is the period of the perturbation, while N is an integer ($-\infty < N < +\infty$) that signifies its harmonic order. The period-averaged change in the refractive index has to be taken into account since it alters the effective index n_{eff} of a mode.

Combining Eqs. (4.2.15) and (4.2.17), the total material polarization is

$$P = \varepsilon_0\left\{n^2 - 1 + 2n\overline{\Delta n}\left[1 + \frac{\nu}{2}\left(e^{i[(2\pi N/\Lambda)z + \phi(z)]} + cc\right)\right]\right\}E_\mu, \tag{4.2.18}$$

where the first term on the RHS is the permittivity, the second term is the *dc* refractive index change, and the third term is the *ac* refractive index modulation. Finally, defining a new modulation amplitude by incorporating the visibility,

$$\delta n(z) = 2n\left[\overline{\Delta n} + \frac{\Delta n}{2}\left(e^{i[(2\pi N/\Lambda)z + \phi(z)]} + cc\right)\right], \tag{4.2.19}$$

with $\Delta n = \nu\overline{\Delta n}$ as the amplitude of the ac refractive index modulation. Equation (4.2.19) describes the UV-induced refractive index change due to a grating written into the fiber core. Figure 4.1 shows the refractive index modulation for a uniform grating on a background index of the core

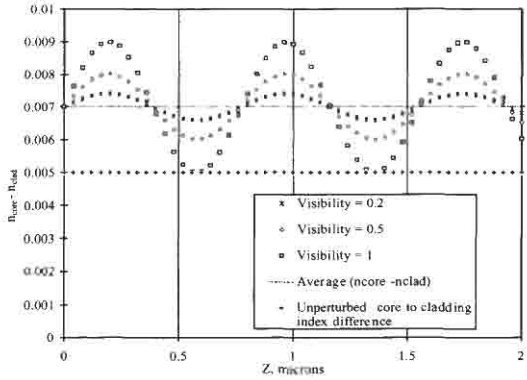

Figure 4.1: Refractive index modulation in the core of a fiber for different visibilities of the fringe pattern. Also shown is the average refractive index change in the core (dashed line). The unperturbed core-to-cladding refractive index difference is 5×10^{-3}, while the maximum refractive index modulation for unity visibility is $\pm 2 \times 10^{-3}$.

of the fiber for different visibilities. Also shown is the effect on the average core index. Note that the change in the average index in the core is constant, irrespective of the visibility of the fringes, although it remains a function of δn. In the example shown, however, both the average index and the refractive index modulation δn increase with UV exposure time.

The perturbed polarization can now be related to refractive index change shown in Eq. (4.2.19) to give

$$P_{pert} = 2n\varepsilon_0\left[\overline{\Delta n} + \frac{\Delta n}{2}\left(e^{i[(2\pi N/\Lambda)z+\phi(z)]} + cc\right)\right]E_\mu. \qquad (4.2.20)$$

Including Eq. (4.2.20) in Eq. (4.2.13) results in

$$\begin{aligned}
&\left[\frac{\partial A_\upsilon}{\partial z}e^{i(\omega t-\beta_\upsilon z)} + cc\right] - \left[\frac{\partial B_\mu}{\partial z}e^{i(\omega t+\beta_\mu z)} + cc\right] \\
&= +\frac{i\varepsilon_0}{2\omega}\int_{-\infty}^{+\infty}\int_{-\infty}^{+\infty}\frac{\partial^2}{\partial t^2}\delta n(z)\left[A_\upsilon e^{i(\omega t-\beta_\upsilon z)}\xi_{\upsilon t} + B_\mu e^{i(\omega t+\beta_\mu z)}\xi_{\mu t}\right]\xi^*_{\mu,\upsilon t}\,dxdy + cc \\
&= -in\omega\varepsilon_0 A_\upsilon\int_{-\infty}^{+\infty}\int_{-\infty}^{+\infty}\left[\overline{\Delta n} + \frac{\Delta n}{2}(e^{i[(2\pi N/\Lambda)z+\phi(z)]} + cc)\right]\xi_{\upsilon t}e^{i(\omega t-\beta_\upsilon z)}\xi^*_{\mu,\upsilon t}\,dxdy \\
&\quad -in\omega\varepsilon_0 B_\mu\int_{-\infty}^{+\infty}\int_{-\infty}^{+\infty}\left[\overline{\Delta n} + \frac{\Delta n}{2}(e^{i[(2\pi N/\Lambda)z+\phi(z)]} + cc)\right]\xi_{\mu t}e^{i(\omega t+\beta_\mu z)}\xi^*_{\mu,\upsilon t}\,dxdy + cc.
\end{aligned} \qquad (4.2.21)$$

On the LHS of Eq. (4.2.21), the rate of variation of either A_v or B_μ is determined by the mode order μ or v of the electric field $\xi^*_{\mu,vt}$ chosen as the multiplier according to the orthogonality relationship of Eq. (4.1.15). This was shown in Eq. (4.2.9) for the case of the single field. Once the term on the LHS has been chosen, the next question is the choice of the terms on the RHS. Before this is examined, we consider the terms on the RHS in general.

The RHS of Eq. (4.2.21) has two generic components for both A and B modes as

$$\begin{aligned} RHS = & -in\omega\varepsilon_0 B_\mu e^{i(\omega t+\beta_\mu z)} \times \int_{-\infty}^{+\infty}\int_{-\infty}^{+\infty} \overline{\Delta n}\,\xi_{\mu t}\xi^*_{\mu t}\,dxdy \\ & -in\omega\varepsilon_0 A_v e^{i(\omega t-\beta_p z+\phi(z))} \times \int_{-\infty}^{+\infty}\int_{-\infty}^{+\infty} \frac{\Delta n}{2}\,\xi_{vt}\xi^*_{\mu t}\,dxdy + cc, \end{aligned} \tag{4.2.22}$$

where the first exponent must agree with the exponent of the generated field on the LHS of Eq. (4.2.21) and has a dependence on the dc refractive index change, $\overline{\Delta n}$. The reason is that any other phase-velocity dependence (as for other coupled mode) will not remain in synchronism with the generated wave. The second term on the RHS has two parts. The first one is dependent on the phase-synchronous factor,

$$\beta_p = \frac{2\pi N}{\Lambda} \pm \beta_v. \tag{4.2.23}$$

The mode interactions that can take place are determined by the right-hand sides of Eqs. (4.2.21) and (4.2.22). Two aspects need to be taken into account: first, conservation of momentum requires that the phase constants on the LHS and the RHS of Eq. (4.2.22) be identical [Eq. (4.2.23)] and so influences the coupling between copropagating or counterpropagating modes. Secondly, the transverse integral on the RHS of Eq. (4.2.22), which is simply the overlap of the refractive-index modulation profile and the distributions of the mode fields, determines the strength of the mode interactions. Let us first consider the conservation of momentum, otherwise known as phase matching.

4.2.2 Phase matching

We begin with Eq. (4.2.23) in which the phase factor is the sum or difference between the magnitude of the driving electric-field mode propagation

constant β_v and the phase factor of the perturbation. The resultant β_p is the phase constant of the induced polarization wave. This is the propagation constant of a "boundwave" generated by the polarization response of the material due the presence of sources. For there to be any significant transfer of energy from the driving field amplitude A_v to the generated fields on the LHS of Eq. (4.2.22), the generated and the polarization waves must remain in phase over a significant distance, z. For continuous transfer of energy,

$$\beta_\mu = \beta_p. \tag{4.2.24}$$

Equation (4.2.24) then describes the phase-matching condition. A phase mismatch $\Delta\beta$ is referred to as a detuning,

$$\Delta\beta = \beta_\mu - \beta_p. \tag{4.2.25}$$

Including Eq. (4.2.23) in (4.2.25), we get,

$$\Delta\beta = \beta_\mu \pm \beta_v - \frac{2\pi N}{\Lambda}. \tag{4.2.26}$$

If both β_v and β_μ have identical (positive) signs, then the phase-matching condition is satisfied ($\Delta\beta = 0$) for counterpropagating modes; if they have opposite signs, then the interaction is between copropagating modes.

Identical relationships for co- and counterpropagation interactions apply to radiation mode phase matching. A schematic of the principle of phase matching is shown in Fig. 4.2.

Finally, energy conservation requires that the frequency ω of the generated wave remains unchanged.

4.2.3 Mode symmetry and the overlap integral

The orthogonality relationship of Eq. (4.1.15) suggests that only modes with the same order μ will have a nonzero overlap. However, the presence of a nonsymmetric refractive index modulation profile across the photosensitive region of the fiber can alter the result, allowing modes of different orders to have a nonzero overlap integral. The reason for this fundamental departure from the normalization of Eq. (4.1.15) is the nonuniform *transverse* distribution of sources, giving rise to a polarization wave that has an allowed odd symmetry. This is graphically displayed in Fig. 4.3: A driving fundamental mode (LP_{01}, $\mu = 0$) electric field, ξ_v, interacts with

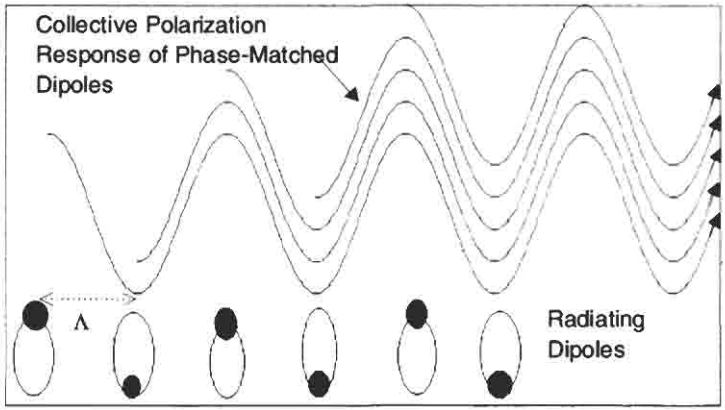

Figure 4.2: The principle of phase matching. The polarization wave grows in synchronism with the driving field. The radiating dipoles are shown to be spatially distributed with a period of Λ, allowing the radiated wave to remain in phase with the driving field. This schematic applies to guided or radiation-mode coupling.

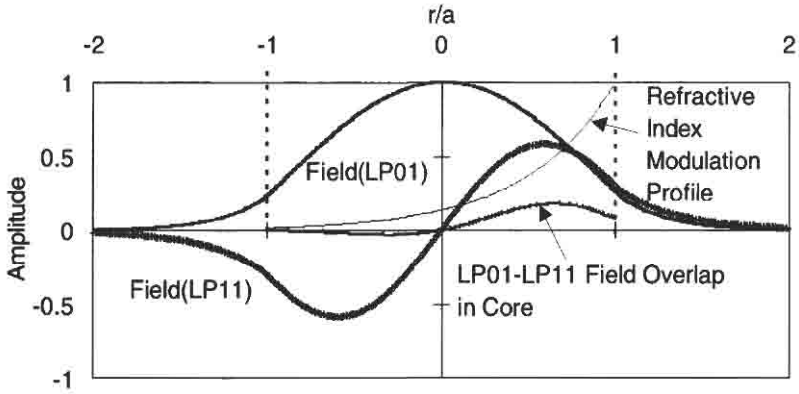

Figure 4.3: A cross-section of the fiber showing the fields of the LP_{01} and the LP_{11} modes, along with the transverse refractive index modulation profile. The overlap of the two fields with the profile of the index modulation [as per Eq. (4.2.22)] changes sign across the core but does not have with the same magnitude. The field overlap is therefore nonzero. The transverse profile of the refractive index thus influences the symmetry of the modes allowed to couple. The transverse profile of the perturbation is equivalent to a "blaze" across the core (tilted grating), which benefits coupling to odd-order radiation modes as well. The two dashed lines indicate the core boundary.

a modulated permittivity that has a uniform transverse profile. Also shown is a polarization field that is in the LP_{11} mode ($v = 1$). Examining the transverse overlap (which is proportional to the product of the field amplitudes and the refractive-index profile) on the left half of the core, we find that magnitude is the same as on the right half, but they have the opposite signs, resulting in a zero overlap. The orthogonality relationship holds and exchange of energy is not possible between the different order modes. If, however, the refractive index profile is not uniform across the core (Fig. 4.3), then although the signs of the overlap in the two halves (around a plane through the axis of the fiber) are different, the magnitudes are no longer identical.

Thus, the overlap is now not zero, allowing a polarization wave to exist with a symmetry (and therefore, mode-order) different from that of the driving mode. The selection rules for the modes involved in the exchange of energy are then determined by the details of the terms in the integral in Eq. (4.2.22) and apply equally to radiation mode orders.

The consequence of the asymmetric refractive index perturbation profile may now be appreciated in Eq. (4.2.21). On the RHS, the integrals with the electric fields of the driving field $\xi_{\mu t}$ and the polarization wave ξ_{vt} along with the asymmetric profile of the refractive index modulation are nonzero for dissimilar mode orders, i.e., $\mu \neq v$. The magnitude of the overlap for a particular mode combination will depend on the exact details of the perturbation profile.

4.2.4 Spatially periodic nonsinusoidal refractive index modulation

Note that in Eq. (4.2.21), the refractive-index perturbation can have a $\pm$ sign in the exponent. This is a direct result of the Fourier expansion of the permittivity perturbation. However, since it is equivalent to an additional momentum, which can be either added to or taken away from the momentum vector of a driving field, it may be viewed as a factor that can take place, as already discussed.

In the general case when the refractive index modulation is not simply sinusoidal but a periodic complex function of z, it is more convenient to expand δn in terms of Fourier components as

$$\delta n(z) = 2n\left[\overline{\Delta n} + \frac{\Delta n}{2}\sum_{N=-\infty}^{N=+\infty} \alpha_N (e^{i[(2\pi N/\Lambda)z + \phi(z)]} + cc)\right], \quad (4.2.27)$$

where α_N is the Fourier amplitude coefficient of the Nth harmonic of the perturbation. Differently shaped periodic functions have their corresponding α_N coefficients, which in turn influence the magnitude of the overlap integral, and hence the strength of the mode coupling.

4.2.5 Types of mode coupling

The phase-matching condition is defined by setting $\Delta\beta$ in Eq. (4.2.26) to zero. Therefore,

$$\beta_v = \pm\left(\frac{2\pi N}{\Lambda} - \beta_\mu\right). \tag{4.2.28}$$

Equation (4.2.28) states that a mode with a propagation constant of β_μ will be synchronously drive another mode A_v with a propagation constant of β_v, provided, of course, the latter is an allowed solution to the unperturbed wave equation (4.1.28) for guided modes and its equivalent for radiation modes.

The guided modes of the fiber have propagation constants that lie within the bounds of the core and the cladding values, although only solutions to the eigenvalue Eq. (4.1.28) are allowed. Consequently, for the two lowest order modes of the fiber, LP_{01} and LP_{11}, the propagation constants β_v and β_μ are the radii of the circles $2\pi n_v/\lambda$ and $2\pi n_\mu/\lambda$. A mode traveling in the forward direction has a mode propagation vector $\overline{K}_{LP_{01}}$ that combines with the grating vector $\overline{K}_{grating}$ to generate $\overline{K}_{result}$. Since the grating vector is at an angle θ_g to the propagation direction, and the allowed mode solution, $\overline{K}_{LP_{11}}$ is in the propagation direction, the phase-matching condition reduces to

$$\Delta\beta = |\beta_{LP_{01}}| + |\beta_{LP_{11}}| - \overline{K}_{grating} \cos\theta_g, \tag{4.2.29}$$

Under these circumstances, the process of phase matching reverses in sign after a distance (known as the coherence length l_c) when

$$\Delta\beta l_c = \pi. \tag{4.2.30}$$

Consequently, the radiated LP_{11} mode (traveling with a phase constant of β_μ) propagates over a distance of l_c before it slips exactly half a wavelength out of phase with the polarization wave (traveling with a phase constant β_v).

In order to understand the various phase-matching conditions, we shall begin with the dispersion diagram of modes. The propagation constants of modes and their dispersion is crucial to the understanding of phase matching. To facilitate an insight into the properties of modes, we use the approximate analogy between rays and modes, since the visual aspect of rays is easier to understand. In Fig. 4.4 we see a section of an optical fiber with a ray incident at the angle at which it is refracted out of the fiber core to exit in a direction parallel to the z-axis. The propagation direction is indicated as the z-axis while the transverse direction is the x-axis. The angle $\theta_{critical} = \sin^{-1}(n_{clad}/n_{core})$is marked as the critical angle for that ray. The ray propagation angle is θ_{cutoff}. Thus, all ray angles below θ_{cutoff} are allowed, but only those that form standing waves [2] exhibit mode properties, with a specific effective propagation index n_{eff}. We note an important relationship in the ray picture: Since the effective index of at mode at cut-off is the cladding refractive index, the effective index of a mode *is the cutoff index of a mode propagating in a waveguide with a cladding refractive index of* n_{eff}.

We now transfer this picture to the one shown in Fig. 4.5. Three circles with radii n_0, n_{clad}, and n_{core} form the boundaries for the waveguide.

Figure 4.5 shows the generalized dispersion diagram for an optical fiber. The outer circle has a radius of n_{core}, the middle circle has a radius of n_{clad}, and the shaded circle represents free space and has a radius of unity. It is based on the ray diagram shown in Fig. 4.4, so that the critical angle for the backward-propagating guided modes is marked as $\theta^m_{critical}$ between the dotted and the dashed lines at point G^m_b, with a similar angle at G^m_f for the forward-propagating modes. The two vertical dotted lines

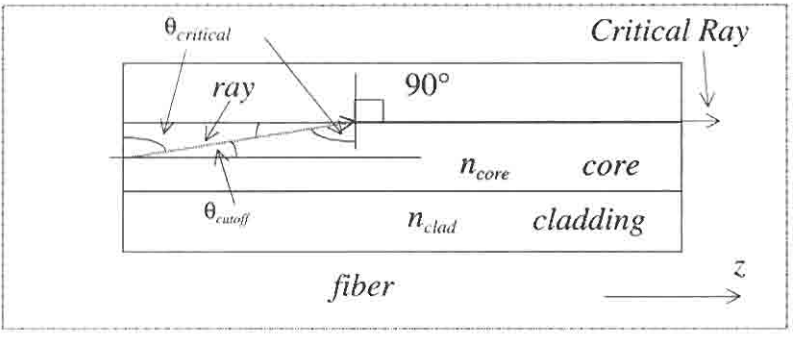

Figure 4.4: Ray propagation in a waveguide.

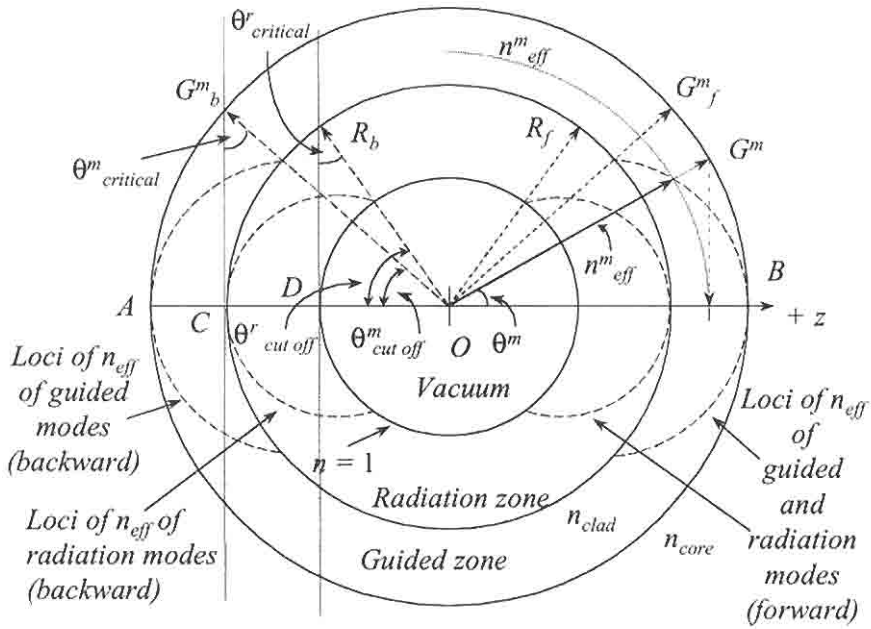

Figure 4.5: Generalized dispersion diagram for guided and radiation modes and radiation field for waveguides.

are tangential to the cladding and inner circles, respectively. All guided modes have their cutoff at $\theta^m_{critical}$. The equivalent cutoff angles in the propagation direction for all guided modes are also marked at the origin, as θ^m_{cutoff}.

For the radiation (cladding) modes the equivalent angles are $\theta_{critical}$ and θ_{cutoff}, subtended by the dashed lines to points R_b and R_f. The dashed lines in Fig. 4.5 mark these. We note that all guided modes have effective indexes lying within the region bounded by the outer two circles. A forward-propagating guided mode has an effective index of n^m_{eff}, which lies on a circle of radius n^m_{eff} (part of a dashed circle is shown) and on a vector OG^m, propagating at an angle θ^m to the z-axis. It is easy to show that the loci of all the effective indexes of the (forward- and backward-propagating) modes lie on circles (shown as the outer two dashed circles). The length of the vector from the origin to the intercept with the n^m_{eff} circle subtends the ray angle θ^m for that mode. The point at which these dashed circles meet the n_{clad} circle defines the cutoff of the guided modes. A

similar set of circles intersects the free space shaded inner circle to define the cutoff of *all* cladding modes. Beyond this point and into the inner shaded circle is the radiation field region. If the cladding were extended to infinity, the middle circle would become the locus of *all* cladding space modes (continuum). In the present situation, the inner circle remains the locus of the free space modes, which are the cladding modes beyond cutoff.

Having defined the phase space for all the modes, we can proceed to the phase-matching diagram, shown in Fig. 4.6. Here we see a forward-propagating mode, with an effective index of $n_{core}\cos\theta_f^n$, phase matched to a counterpropagating mode with an effective index of $n_{core}\cos\theta_b^n$ (point G_{pm}) with a grating that has an "effective index" of $n_g\cos\theta_g$. The grating period $\Lambda_g = \lambda/(n_g\cos\theta_g)$. When $\theta_g = 0$, we have the normal Bragg condition. We can now see the effect of detuning this interaction to shorter wavelengths. The point G^m moves down toward B, dragging the grating vector n_g with it. This action carves out a phase-matching curve on the LH side of the figure, marked by the dashed curve. Phase matching is lost since

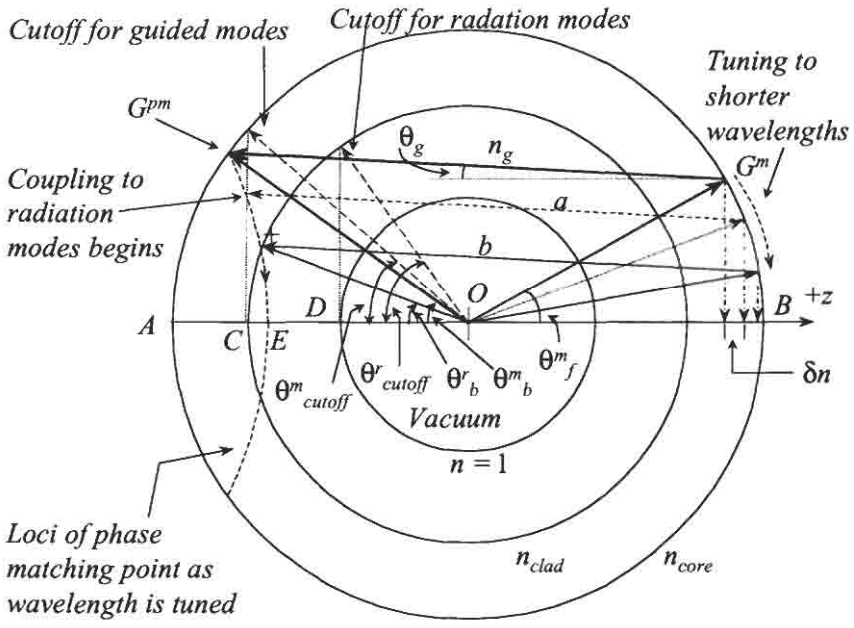

Figure 4.6: Guided mode and radiation mode/field phase-matching diagram for the slanted Bragg grating (counterradiating coupling).

there is no intersection with the outer or inner circles. There is a gap in the spectrum, in which no phase matching is possible. At some point the arrowhead meets the vertical dotted line for the radiation modes on line a, and phase matching to the radiation modes begins. This will couple to the lowest-order modes. With an infinite cladding, free-space radiation mode phase matching occurs. As the wavelength becomes even shorter, the angle of the radiation modes increases, and only when the vector b meets the n_{clad} circle is radiation mode coupling at an angle of θ_b. After this point, the angle of the radiation mode increases beyond θ_b. We now note that the change in the mode index is δn from the RH side of the figure, so that we can calculate the wavelength at which the radiation loss starts to occur.

Figure 4.6 shows the phase-matching diagram for coupling to the guided and radiation modes and fields with a tilted grating, known as *side-tap-grating* (STG, also see Chapter 6). This grating has a period similar to Bragg gratings but does not have its grating planes normal to the fiber axis, and it is tilted at an angle, θ_g. The diagram specifically deals with the case of coupling to counterpropagating fields.

In the first interaction with n_g, we have Bragg reflection at λ_{Bragg}. We assume that the grating angle $\theta_g = 0$, and that when the wavelength is tuned, the effective index of the mode is n_{eff}^{start} at the point indicated by a on Fig. 4 6, so that mathematically, this is simply phase matching to a mode with the cladding index as

$$\frac{2\pi n_{eff}^{start}}{\lambda_{start}} + \frac{2\pi n_{clad}^{start}}{\lambda_{start}} = \frac{2\pi N}{\Lambda_g} = \frac{4\pi n_{eff}^{Bragg}}{\lambda_{Bragg}}, \tag{4.2.31}$$

where *start* indicates the wavelength at which the radiation mode coupling begins.

Rearranging and using the approximation $n_{eff} \approx n_{eff}^{start} \approx n_{eff}^{Bragg}$, it follows that

$$\lambda_{start} = \frac{\lambda_{Bragg}}{2}\left(1 + \frac{n_{clad}}{n_{eff}}\right). \tag{4.2.32}$$

Therefore, radiation loss begins at a wavelength slightly shorter than the Bragg wavelength, governed by the ratio in the brackets in Eq. (4.2.32). For example, in a fiber with a large core–cladding index difference with a tightly confined Bragg wavelength (1550 nm) mode ($n_{eff} = 1.475$), the start wavelength will be at ~1537 nm, some 13 nm away.

We can estimate the maximum angle for the radiation by observing the point E on the phase-matching curve in Fig. 4.6. The tangent to this point on the phase matching at E intersects the cladding circle at the "+" point. This point subtends the largest radiation mode angle for this particular grating, at the origin. The maximum angle of the radiation for an untilted grating is at the shortest wavelength and is easily shown to be

$$\theta'_{\max} = \cos^{-1}\left(\frac{2n_{eff} - n_{core}}{n_{clad}}\right), \tag{4.2.33}$$

which is maximum if $n_{eff} = n_{clad}$. For a core-to-cladding refractive index difference of 0.01 in a silica fiber, $\theta'_{max} \approx 6.7°$. It should be remembered that phase matching to specific radiation *modes* will only occur if a cladding mode exists with the appropriate mode index. However, with an infinite cladding, coupling to a continuum of the radiation field occurs so that the spectrum is continuous.

There is another possibility for coupling to radiation modes. We begin with $\theta_g = 0$ and the condition for Bragg reflection from, for example, the forward to the counterpropagating LP_{01} mode. If the grating is tilted at an angle θ_g, it is shown simply as a rotation of n_g around the pivot at G^m. Following the mathematical approach taken for Eq. (4.2.33), we find that at some angle θ'_g the radiation mode is at the Bragg wavelength, i.e., the start wavelength moves toward the Bragg wavelength, until they coincide. At this point, there is strong coupling to the radiation modes. Referring to Fig. 4.6, the angle is easily found by changing the tilt of the grating. This directly leads to

$$K_g - K_g \cos \theta'_g = \frac{4\pi}{\lambda_{Bragg}} (n_{eff} - n_{clad}), \tag{4.2.34}$$

where n_{eff} is the effective index of the mode at the Bragg wavelength of the untilted grating (when $\theta_g = 0$), so that

$$\cos \theta'_g = \frac{n_{clad}}{n_{eff}}. \tag{4.2.35}$$

Again, the tilt angle of the grating for this condition to be met increases with n_{eff} and is a maximum when $n_{eff} = n_{core}$. We can calculate

that for a standard fiber, with an $n_{eff} \approx n_{clad} + b\Delta n$ ($\delta n = 4.5 \times 10^{-3}$) and $b = 0.4$ at 1550 nm [2], the angle at which the Bragg wavelength equals the radiation wavelength is $\theta_g' \approx 2.85°$. It is clear from Eq. (4.2.35) that the angle becomes larger with increasing core–cladding index difference.

Finally there is a set of unconfined radiation modes at a continuum of angles subtended at O, but with vector lengths within the space of the radiation zone. Making the grating "effective index" n_g small so that the arrowhead remains on the RH side of Fig. 4.6, one can see that phase matching will occur between copropagating modes, or to radiation modes in the forward direction. This is better shown in Fig. 4.7.

The following points should be noted regarding the phase-matching diagram. The guided mode propagation constants have discrete values and lie on the loci for the particular mode propagation constants. The grating vector can have any angle θ_g to the propagation direction, as can the radiated field, provided the cladding is assumed to be at infinity. If,

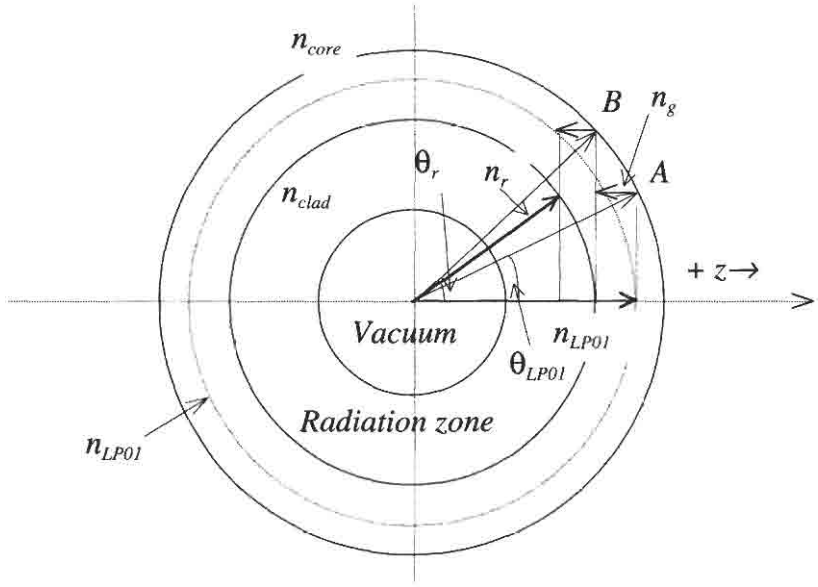

Figure 4.7: The phase-matching diagram for copropagating modes with radiation mode coupling with a long-period grating.

however, a cladding boundary is present as shown by the innermost dashed circle, then the radiated modes only have allowed β-values. This radiation may be viewed as the modes of a waveguide with a core of refractive index n_{clad} and a radius equal to the fiber-cladding radius surrounded by an infinite cladding of air/vacuum refractive index. The diagram then acquires a set of circles with radii $n_{vacuum} < n_\rho < n_{clad}$ representing discrete *cladding* modes, similar to those for guided modes, at the points of intersection with the dispersion curves. The radiation mode fields are slightly modified by the presence of the high-index fiber core.

Coupling is also possible to the forward-radiating modes and fields. This requires a different grating, known as a long-period grating, which has a much longer period than a Bragg grating, since the momentum of the mode does not change sign (as in forward-to-backward coupling). The phase matching for the generalized case of the tilted grating for copropagating coupling is shown in Fig. 4.7. The form of the diagram is similar to Figs. 4.5 and 4.6.

For phase matching, the movement of the n_g arrowhead for the LPG is opposite to that of the STG. We begin with an LP_{01} mode with the propagation index arrow $n_{LP_{01}}$ pointing in the $+z$ direction. The grating n_g starts at the tip of the guided mode arrow, inclined at $\theta_g = 0$ to the fiber axis. The wavelength at which radiation is first emitted is when the tip of the grating vector from point A intersects the tangent to the cladding mode circle (dashed vertical line). This point represents the longest-wavelength LP_{01} mode that has a propagation constant equal to the cladding index and has the lowest angle. Light is coupled to radiation modes within the radiation zone as n_g is moved to the left and *the LP_{01} mode is "cut off" at the radiation angle*, θ_r. Therefore, θ_r is the angular spread of the radiated fields. Mode coupling is only possible if there is phase matching to specific modes. Note that this wavelength approaches ∞, since the fundamental guided mode effective index approaches n_{clad}. The wavelength vs angle has the opposite dependence of the STG, i.e., long wavelengths exit at the largest angle in the LPG, while it is the shortest wavelengths in the STG. The first Bragg wavelength reflection (very weak) is at the *short* wavelength side of the LPG radiation loss spectrum, while it is on the *long* wavelength side of the STG radiation loss spectrum. The spectrum of the LPG is "reversed" around the Bragg wavelength.

Figure 4.8 shows various types of phase-matched interactions possible with different types of gratings.

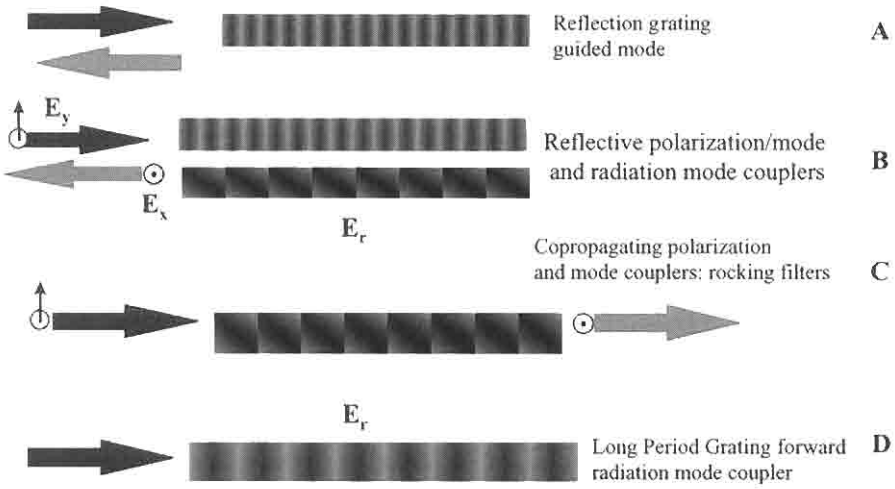

Figure 4.8: Types of Bragg gratings categorized by action of coupling. The schematics show various gratings in the core of an optical fiber. All gratings are shown to be transversely uniform. A nonuniform transverse refractive index modulation profile enhances coupling to either different mode orders of guided or to the radiation field. ***A*** shows a guided mode reflection grating. ***B*** shows a reflecting guided mode polarization coupler, mode converter, or radiation mode coupler ("side-tap" grating). ***C*** is a polarization coupler for copropagating modes, also knows as a "rocking filter" [31]. ***D*** is the copropagating guided-mode to radiation-mode coupler, also known as the "long-period grating."

4.3 Coupling of counterpropagating guided modes

The simplest form of interaction is between a forward-propagating and an identical backward-propagating mode. However, for a general approach, dissimilar modes are considered for the counterpropagating (reflected) mode phase matching with Eq. (4.2.21) rewritten as

$$\frac{\partial B_\mu}{\partial z} e^{i(\omega t+\beta_\mu z)} + cc = in\omega\varepsilon_0 B_\mu \int_{-\infty}^{+\infty}\int_{-\infty}^{+\infty} \overline{\Delta n}\,\xi_{\mu t}\xi_{\mu t}^{*} e^{i(\omega t+\beta_\mu z)}\,dxdy$$
$$+ in\omega\varepsilon_0 A_v \int_{-\infty}^{+\infty}\int_{-\infty}^{+\infty} \frac{\Delta n}{2} e^{i[(2\pi N/\Lambda)z+\phi(z)]}\xi_{vt}\xi_{\mu t}^{*} e^{i(\omega t-\beta_v z)}\,dxdy + cc. \tag{4.3.1}$$

By choosing the appropriate β value for identical modes ($\mu = v$) but with opposite propagation directions in Eq. (4.3.1) and dividing both sides by $\exp[i(\omega t + \beta_\mu z)]$,

$$\begin{aligned}\frac{\partial B_\mu}{\partial z} &= in\omega\varepsilon_0 B_\mu \int_{-\infty}^{+\infty}\int_{-\infty}^{+\infty} \overline{\Delta n}\,\xi_{\mu t}\xi_{\mu t}^{*}\,dxdy \\ &\quad + in\omega\varepsilon_0 A_v \int_{-\infty}^{+\infty}\int_{-\infty}^{+\infty} \frac{\Delta n}{2}\, e^{i([(2\pi N/\Lambda)-\beta_v-\beta_\mu]z+\phi(z))}\xi_{vt}\xi_{\mu t}^{*}\,dxdy,\end{aligned} \tag{4.3.2}$$

which leads to the following simple coupled-mode equations by choosing the appropriate synchronous terms,

$$\frac{\partial B_\mu}{\partial z} = i\kappa_{dc}B_\mu + i\kappa_{ac}A_v e^{-i(\Delta\beta z-\phi[z])}, \tag{4.3.3}$$

with

$$\Delta\beta = \beta_\mu + \beta_v - \frac{2\pi N}{\Lambda}, \tag{4.3.4}$$

and the dc coupling constant,

$$\kappa_{dc} = n\omega\varepsilon_0 \int_{-\infty}^{+\infty}\int_{-\infty}^{+\infty} \overline{\Delta n}\,\xi_{\mu t}\xi_{\mu t}^{*}\,dxdy, \tag{4.3.5}$$

while the *ac* coupling constant κ_{ac} includes the overlap integral,

$$\begin{aligned}\kappa_{ac} &= n\omega\varepsilon_0 \int_{-\infty}^{+\infty}\int_{-\infty}^{+\infty} \frac{\Delta n}{2}\,\xi_{vt}\xi_{\mu t}^{*}\,dxdy \\ &= \frac{v}{2}\,\kappa_{dc},\end{aligned} \tag{4.3.6}$$

if $\mu = v$. The change in the amplitude of the driving mode may also be derived from Eq. (4.2.21) as

$$\frac{\partial A_v}{\partial z} = -i\kappa_{dc}A_v - i\kappa_{ac}^{*}B_\mu e^{i(\Delta\beta z-\phi(z))}. \tag{4.3.7}$$

Eqs. (4.3.3) and (4.3.7) are the coupled-mode equations from which the transfer characteristics of the Bragg grating can be calculated.

To find a solution, the following substitutions are made for the forward (reference) and backward propagating (signal) modes [32]:

$$\begin{aligned} R &= A_v e^{-(i/2)[\Delta\beta z - \phi(z)]} \\ S &= B_\mu e^{(i/2)[\Delta\beta z - \phi(z)]}. \end{aligned} \tag{4.3.8}$$

Differentiating Eq. (4.3.8) and substituting into Eqs. (4.3.3) and (4.3.7) results in the following coupled-mode equations:

$$\frac{dR}{dz} + i\left[\kappa_{dc} + \frac{1}{2}\left(\Delta\beta - \frac{d\phi(z)}{dz}\right)\right]R = -i\kappa_{ac}^* S \tag{4.3.9}$$

$$\frac{dS}{dz} - i\left[\kappa_{dc} + \frac{1}{2}\left(\Delta\beta - \frac{d\phi(z)}{dz}\right)\right]S = i\kappa_{ac} R. \tag{4.3.10}$$

The physical significance of the terms in brackets is as follows: κ_{dc} influences propagation due to the change in the average refractive index of the mode, as has already been discussed. Any absorption, scatter loss, or *gain* can be incorporated in the magnitude and sign of the imaginary part of κ_{dc}. Gain in distributed feedback gratings will be discussed in Chapter 8. There are also two additional terms within the parentheses in Eqs. (4.3.9) and (4.3.10), the first one of which, $\Delta\beta/2$, is the detuning and indicates how rapidly the power is exchanged between the "radiated" (generated) field and the polarization ("bound") field. This weighting factor is proportional to the inverse of the distance the field travels in the generated mode. At phase matching, when $\Delta\beta = 0$, the field couples to the generated wave over an infinite distance Finally, the rate of change of ϕ signifies a chirp in the period of the grating and has an effect similar to that of the detuning. So, for uniform gratings, $d\phi/dz = 0$, and for a visibility of unity for the grating, $\kappa_{ac} = \kappa_{dc}/2$.

The coupled-mode Eqs. (4.3.9) and (4.3.10) are solved using standard techniques [33]. First the eigenvalues are determined by replacing the differential operator by λ and solving the characteristic equation by equating the characteristic determinant to zero. The resultant eigenvalue equation is in general a polynomial in the eigenvalues λ. Once the eigenvalues are found, the boundary values are applied for uniform gratings: We assume that the amplitude of the incident radiation from $-\infty$ at the input of a fiber grating (of length L) at $z = 0$ is $R(0) = 1$, and that the field $S(L) = 0$. The latter condition is satisfied by the fact that the reflected field at the output end of the grating cannot exist owing to the absence of the

perturbation beyond that region. These conditions result in the following analytical solution for the amplitude reflection coefficient:

$$\rho = \frac{S(0)}{R(0)} = \frac{-\kappa_{ac} \sinh(\alpha L)}{\delta \sinh(\alpha L) - i\alpha \cosh(\alpha L)}, \tag{4.3.11}$$

where

$$\delta = \kappa_{dc} + \frac{1}{2}\left(\Delta\beta - \frac{d\phi(z)}{dz}\right) \tag{4.3.12}$$

and

$$\alpha = \sqrt{|\kappa_{ac}|^2 - \delta^2}. \tag{4.3.13}$$

A few points regarding Eqs. (4.3.9)–(4.3.13) are worth mentioning. First, for reflection gratings that have a constant period Λ, the variation in the phase $d\phi(z)/dz = 0$. Second, at precise phase matching, $\Delta\beta = 0$, and the ac coupling constant κ_{ac} is a real quantity. Finally, the power reflection coefficient is $|\rho|^2$,

$$|\rho|^2 = \frac{|\kappa_{ac}|^2 \sinh^2(\alpha L)}{|\kappa_{ac}|^2 \cosh^2(\alpha L) - \delta^2}, \tag{4.3.14}$$

in which Eq. (4.3.13) has been used to simplify the result. Noting from Eq. (4.3.14) that α can be real or imaginary, the following regimes may be identified:

1. α is real when $|\kappa_{ac}| > \delta$ and Eqs. (4.3.11) and (4.3.14) apply.
2. α is zero when $|\kappa_{ac}| = \delta$.
3. α is imaginary when $|\kappa_{ac}| < \delta$ and Eqs. (4.3.11) and (4.3.14) transform to

$$\rho = \frac{-\kappa_{ac} \sin(\alpha L)}{i\alpha \cos(\alpha L) + \delta \sin(\alpha L)}, \qquad |\kappa_{ac}| < \delta, \tag{4.3.15}$$

and

$$|\rho|^2 = \frac{|\kappa_{ac}|^2 \sin^2(\alpha L)}{\delta^2 - |\kappa_{ac}|^2 \cos^2(\alpha L)}, \qquad |\kappa_{ac}| < \delta. \tag{4.3.16}$$

4.4 Codirectional coupling

In a multimode fiber, coupling can occur between orthogonally polarized modes of the same order, or to cladding modes (LPG) if the transverse

profile of the refractive index perturbation is uniform. However, as has been described by the general mode-coupling constants of Eqs. (4.2.5) and n(4.2.6) dissimilar mode orders that normally cannot couple owing to the orthogonality relationship [Eq. (4.1.15)] are allowed to couple when the transverse profile of the refractive index is nonuniform. This applies equally to copropagating modes. In this case, coupling may normally occur between

1. Copropagating orthogonal polarizations, e.g., $(HE_{11})_{x,y} \leftrightarrow (HE_{11})_{y,x}$ ($LP_{01,x}$ and the $LP_{01,y}$). A uniform grating profile is necessary for good efficiency. To allow coupling between these modes, the grating is written at 45° to the principle birefringent axes of the fiber (see Section 4.5 and Chapter 6).
2. $(LP_{01})_{x,y} \leftrightarrow (LP_{v\mu})_{x,y}$. Here, the transverse profile of the grating strongly influences the strength of the coupling. With a uniform profile, the coupling is zero for $v \neq 0$.
3. Coupling to the radiation field E_ρ (as with LPGs). Since the radiation field is evanescent in the core of the fiber and oscillatory in the cladding, coupling can be strongly influenced if a grating extends into the cladding as well. The latter diminishes the overlap integral between the guided lowest-order mode and the radiation modes, while an asymmetric transverse grating profile can enhance the interaction with odd modes.

Following the analysis developed in Section 4.2 and 4.3, the mode coupling equations for copropagating modes are

$$\frac{\partial B_\mu}{\partial z} = -i\kappa_{dc,\mu}B_\mu - i\kappa_{ac,v\mu}A_v e^{-i(\Delta\beta z - \phi[z])}, \tag{4.4.1}$$

but with the phase-mismatch factor

$$\Delta\beta = \beta_v - \beta_\mu - \frac{2\pi N}{\Lambda}, \tag{4.4.2}$$

and the dc self-coupling constant for each of the modes,

$$\kappa_{dc,\mu} = n\omega\varepsilon_0 \int_{-\infty}^{+\infty}\int_{-\infty}^{+\infty} \overline{\Delta n}\,\xi_{\mu t}\xi_{\mu t}^* \, dxdy \tag{4.4.3}$$

$$\kappa_{dc,v} = n\omega\varepsilon_0 \int_{-\infty}^{+\infty}\int_{-\infty}^{+\infty} \overline{\Delta n}\,\xi_{vt}\xi_{vt}^* \, dxdy. \tag{4.4.4}$$

The cross-coupling constant κ_{ac} remains the same as for contradirectional coupling as

$$\kappa_{ac,\upsilon\mu} = n\omega\varepsilon_0 \int_{-\infty}^{+\infty}\int_{-\infty}^{+\infty} \frac{\Delta n}{2}\, \xi_{\upsilon t}\xi_{\mu t}^{*}\, dxdy. \tag{4.4.5}$$

The amplitude of the input mode evolves as

$$\frac{\partial A_\upsilon}{\partial z} = -i\kappa_{dc,\upsilon}A_\upsilon - i\kappa_{ac,\mu\upsilon}^{*}B_\mu e^{i(\Delta\beta z - \phi(z))}. \tag{4.4.6}$$

Notice that the dc coupling constants may be different for the evolution of the input and coupled modes. To resolve this problem, we introduce new variables, R and S as before, but slightly modified, to result in a common coupling factor:

$$A_\upsilon = \mathrm{Re}^{-i((\kappa_{dc,\mu}+\kappa_{dc,\upsilon})/2)z} \times e^{(i/2)[\Delta\beta z - \phi(z)]} \tag{4.4.7}$$

$$B_\mu = Se^{-i((\kappa_{dc,\mu}+\kappa_{dc,\upsilon})/2)z} \times e^{(-i/2)[\Delta\beta z - \phi(z)]}. \tag{4.4.8}$$

The subscripts μ and υ on the dc coupling constants κ_{dc} are specific to each mode and is defined by Eq. (4.2.5) for identical modes. Differentiating R and S, collecting terms, and substituting into Eqs. (4.4.1) and (4.4.6) leads to

$$\frac{dR}{dz} - \frac{i}{2}\left[\kappa_{dc,\mu} - \kappa_{dc,\upsilon} + \Delta\beta + \frac{d\phi(z)}{dz}\right]R = -i\kappa_{ac}^{*}S \tag{4.4.9}$$

$$\frac{dS}{dz} - \frac{i}{2}\left[\Delta\beta + \kappa_{dc,\upsilon} - \kappa_{dc,\mu} - \frac{d\phi(z)}{dz}\right]S = -i\kappa_{ac}R. \tag{4.4.10}$$

The phase-mismatch factor $\Delta\beta$ is now proportional to the *difference* in the propagation constants of the two modes as shown in Eq. (4.4.2).

The *cross*-coupling constant κ_{ac} is defined by Eqs. (4.2.6) and (4.4.5) as $\kappa_{ac,\mu\upsilon}$ for identical or nonidentical modes. Note that the coupling constant is real so that $\kappa_{ac,\mu\upsilon} = \kappa_{ac,\upsilon\mu}^{*} = \kappa_{ac}$.

The grating transmission function comprises two modes — in the simplest case, two orthogonal modes of the same order. However, the general case includes nonidentical modes (including a radiation mode) with the same or orthogonal polarization. The details of the coupling constants κ_{ac} and κ_{dc} need to be evaluated numerically. Radiation modes are considered in Section 4.7, while coupling between different polarizations is presented in Section 4.5.

The solutions to the coupled-mode Eqs. (4.4.9) and (4.4.10) are found by applying the boundary values as in the case of the reflection grating. However, for the transmission grating, the input fields, $R(-L/2) = 1$ and $S(-L/2) = 0$. The power couples from R to S so that the transmission in the uncoupled state is

$$\frac{|R(L/2)|^2}{|R(-L/2)|^2} = \frac{\delta^2}{\alpha^2}\sin^2(\alpha L) + \cos^2(\alpha L), \tag{4.4.11}$$

and the transmission in the coupled state (also known as the crossed state) is

$$\frac{|S(L/2)|^2}{|R(-L/2)|^2} = \frac{\kappa_{ac}^2}{\alpha^2}\sin^2(\alpha L). \tag{4.4.12}$$

In Eqs. (4.4.11) and (4.4.12), $\alpha = (|\kappa_{ac}|^2 + \delta^2)^{1/2}$, and

$$\delta = \frac{1}{2}\left[\kappa_{dc,v} - \kappa_{dc,\mu} + \Delta\beta - \frac{d\phi(z)}{dz}\right].$$

The difference between reflection as in contradirectional coupling and codirectional mode coupling is immediately apparent according to Eqs. (4.2.14) and (4.4.12). While the reflected signal continues to increase with increasing αL, the forward-coupled mode *recouples* to the input mode at $\alpha L > \pi/2$. Therefore, a codirectional coupler requires careful fabrication for maximum coupling.

Figure 4.9 demonstrates the optimum coupling to the crossed state with $\kappa_{ac}L = \pi/2$ (curve A) as the coupling length doubles, the transmission band becomes narrower (C), while B shows the situation of $\kappa_{ac}L = \pi$, when the light is coupled back to the input mode.

4.5 Polarization couplers: Rocking filters

Equations (4.4.9) and (4.4.10) also govern coupling of modes with orthogonal polarization. An additional subscript is used to distinguish between the laboratory frame polarizations. However, there are differences in the detail of the coupling mechanism. In order to couple two orthogonally polarized modes, the perturbation must break the symmetry of the waveguide. This requires a source term, which can excite the coupled mode. In perfectly circular fibers, any perturbation can change the state of the

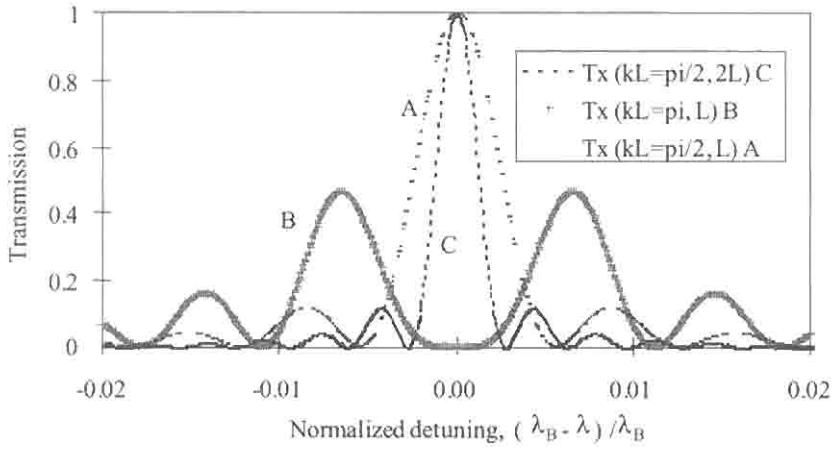

Figure 4.9: Cross-coupled transmission for codirectional coupling. The data shown is for coupling constants of $\pi/2$ with a grating length of L (curve A) and length $2L$ (curve C). The bandwidth is halved for the longer grating. Also shown is data for $\kappa L = \pi$ and grating length L (curve B). Note that the grating overcouples at zero detuning. The transmission spectra of LPGs are identical to that shown above for each of the cladding modes to which the guided mode couples.

output polarization. Nondegenerate orthogonally polarized modes can only exist in birefringent fibers and so require a periodic perturbation equal to the beat length.

Generically, the polarization coupler behaves in a similar way to the intermodal coupler, except that the coupling is between the two eigenpolarization states of the fiber rather than two different order modes. As a result, gratings that have a uniform refractive index modulation across the core are used rather than blazed (or tilted) gratings. Coupling between two dissimilar order modes occurs when symmetry is broken by slanting the grating in the direction of propagation; for coupling between the eigenpolarization states of the same order, symmetry is broken by orienting the grating at 45° to the polarization axes of the fiber. "Slanting" the grating azimuthally at an angle of 45° to the birefringent axes "rocks" the birefringence [34] of the fiber backward and forward, with a period equal to the beat length,

$$\frac{2\pi}{L_b} = \beta_x - \beta_y, \tag{4.5.1}$$

where L_b is the beat length, so that the rocking period Λ_r is

$$\Lambda_r = \frac{L_b}{N}. \tag{4.5.2}$$

N is the order of the grating, and the detuning parameter is

$$\Delta\beta = \beta_x - \beta_y - \frac{2N\pi}{\Lambda_r}. \tag{4.5.3}$$

We assume that the dielectric constants of the principal axes are ε_x and ε_y. A UV beam incident at an angle θ degrees to the x-axis and orthogonal to the propagation direction induces a new set of orthogonal birefringent axes with a change $\Delta\varepsilon_{x'}$ and $\Delta\varepsilon_{y'}$ in the dielectric constants. Figure 4.10 shows the incident UV beam on the cross-section of the fiber. The major and minor axes of the ellipse are the birefringent axes of the fiber. The beam is incident at an angle θ. As a result, the birefringence changes locally, inducing a rotation in the birefringent axes of the fiber. The rotation angle ϕ is related to the change in the birefringence as [35]

$$\tan 2\phi = \frac{\delta\Delta\varepsilon \sin 2\theta}{\Delta\varepsilon + \delta\Delta\varepsilon \cos 2\theta}, \tag{4.5.4}$$

where $\delta\Delta\varepsilon = \Delta\varepsilon_{x'} - \Delta\varepsilon_{y'}$ and $\Delta\varepsilon = \varepsilon_x - \varepsilon_y$. For the case when the induced birefringence is much less than the intrinsic birefringence, then the rotation angle ϕ is small, and it follows that

$$2\phi = \frac{\delta\Delta\varepsilon}{\Delta\varepsilon} \sin 2\theta. \tag{4.5.5}$$

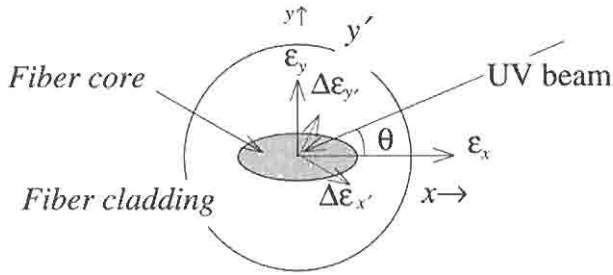

Figure 4.10: Birefringence induced by the incident UV beam in a birefringent fiber for the formation of a rocking filter.

Remembering that $\delta\Delta\varepsilon/\Delta\varepsilon = 2n_{av}(\delta\Delta n')/(2n_{av}\Delta n)$, with $\delta\Delta n' = \Delta n_{x'} - \Delta n_{y'}$,

$$\phi = \frac{1}{2}\frac{\Delta n'}{B}\sin 2\theta, \tag{4.5.6}$$

where B is the difference in the refractive index of the principle axes.

For the special case of $\theta = \pi/4$, Eq. (4.5.6) simplifies to $\phi = \delta\Delta n'/(2B)$. A rotation that changes sign over one beat length implies a change in the rotation of 2ϕ radians per beat length so that the coupling constant, κ_{ac},

$$\kappa_{ac}L_b = 2\phi = \frac{\delta\Delta n'}{B}, \tag{4.5.7}$$

and remembering that $B = \lambda/L_b$ leads to

$$\kappa_{ac} = \frac{\delta\Delta n'}{\lambda}, \tag{4.5.8}$$

where λ is the resonance wavelength. The coupler length L_r is given by the distance at which the input polarization is rotated by $\pi/2$, from which it follows that

$$\kappa_{ac}L_r = \frac{\pi}{2}. \tag{4.5.9}$$

Substituting Eq. (4.5.8) into Eq. (4.5.9), we get the rotation length for 100% polarization conversion as

$$L_r = \frac{\pi\lambda}{2\delta\Delta n'}. \tag{4.5.10}$$

In order to calculate the bandwidth between the first zeroes of the transmission spectrum, we note the argument of Eq. (4.4.12), $\alpha L_r = \pm\pi$, which leads to

$$2\frac{\Delta\lambda}{\lambda} = 2\frac{\pi L_b}{L_r}. \tag{4.5.11}$$

Using typical figures for the reported changes in the birefringence [36,37,35,31], at a wavelength of 1550 nm, we find that the rocking filter has a length of ~0.5 m. Note that the coupler length is only dependent on the wavelength of operation and the induced birefringence, but not

the *intrinsic* birefringence of the fiber. If however, the "duty cycle" of the UV-exposed region is varied so that less than half of a beat length is exposed per beat length, then the effective rocking angle per beat length will be reduced, as with the change in θ.

4.6 Properties of uniform Bragg gratings

Quantities of interest are the bandwidth, $\Delta\lambda$, reflectivity, transmissivity, the variation in the phase ϕ, and the grating dispersion D as a function of detuning.

For the purpose of illustration, Fig. 4.11 shows the reflection spectrum of two Bragg gratings with different coupling constants $\kappa_{ac}L$ of 2 and 8 calculated from Eq. (4.3.16). Note that the central peak is bounded on either side by a number of subpeaks. This feature is characteristic of a uniform-period grating of finite length, with a constant fringe visibility. The abrupt start and end to the grating is responsible for the side structure. In the weak grating limit ($R < 0.2$), the Fourier transform of the variation in the index modulation results in the reflection spectrum [5].

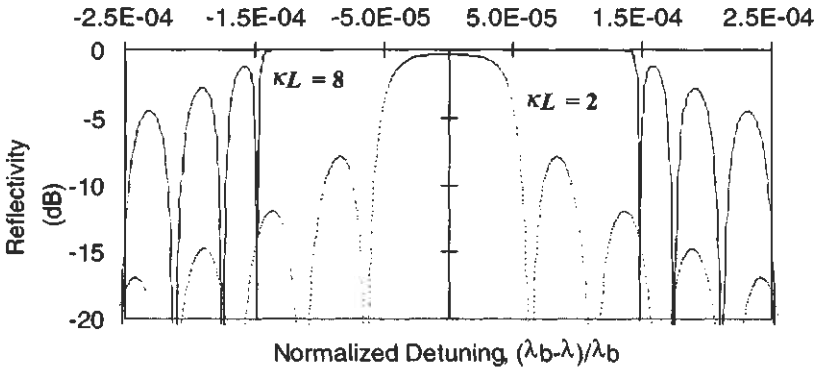

Figure 4.11: Reflectivity of two gratings with coupling constants $\kappa_{ac}L$ of 2 and 8, as a function of normalized detuning. Note that for the weaker reflection grating ($\kappa_{ac}L = 2$, dashed curve), the bandwidth to the first zeroes (between the main reflection peak and the next subpeaks) is much narrower than for the stronger grating ($\kappa_{ac}L = 8$, continuous curve). The side-mode structure increases rapidly for stronger gratings.

Thus, a uniform period and index-modulation grating ("top hat") will produce side lobes. However, for stronger gratings, a Fourier transform for the fundamental component of the refractive index modulation alone is no longer appropriate and gives rise to increasing errors.

For the uniform grating, $d\phi/dz = 0$, the peak reflectivity occurs at a wavelength at which $\delta = 0$ [and therefore, $\alpha = \kappa_{ac}$], and Eq. (4.3.16) leads to

$$\kappa_{dc} + \frac{\Delta\beta}{2} = 0. \tag{4.6.1}$$

At the phase matching wavelength, the reflectivity reduces to

$$|\rho|^2 = \tanh^2(\kappa_{ac}L). \tag{4.6.2}$$

For identical forward- and counterpropagating modes, it is simple to show by using the orthogonality relationship of Eq. (4.1.15) in Eqs. (4.3.5) and (4.3.6) that

$$\kappa_{dc} = \frac{4\pi\eta\overline{\Delta n}}{\lambda}, \tag{4.6.3}$$

where the overlap integral $\eta \approx 1$ for identical modes, and it therefore follows that the peak of the Bragg reflection is at

$$\lambda_{\max} = \lambda_B\left(1 + \frac{\eta\overline{\Delta n}}{n}\right). \tag{4.6.4}$$

The Bragg wavelength λ_B is defined at the phase-matching point $\Delta\beta = 0$ for the general case of dissimilar modes,

$$\frac{2\pi}{\Lambda} = \frac{2\pi n_{eff,v}}{\lambda} + \frac{2\pi n_{eff,\mu}}{\lambda}, \tag{4.6.5}$$

with the result

$$\Lambda = \frac{\lambda}{n_{eff,v} + n_{eff,\mu}}. \tag{4.6.6}$$

For identical forward- and counterpropagating modes or nearly identical mode indexes, Eq. (4.6.6) reduces to

$$\Lambda = \frac{\lambda_{Bragg}}{2n_{eff}}. \tag{4.6.7}$$

The reason why the reflection peak is at a longer wavelength than the Bragg wavelength is because the average refractive mode index $\overline{\Delta n}$ continuously increases with a positive refractive index modulation.

For nonidentical modes, the integral in Eq. (4.3.5) has to be integrated numerically. However, the integral is simply a weighting factor, $0 < \eta < 1$, dependent on the mode and refractive index profiles. It is for this reason that η has been introduced in Eq. (4.6.3), normalized to unity for identical modes.

There are several definitions of bandwidth. However, the most easily identifiable one is bandwidth between the first minima on either side of the main reflection peak (with reference to Fig. 4.11). This may be calculated by equating the argument αL in Eq. (4.3.11) to π,

$$\alpha L = \sqrt{\kappa_{ac}^2 - \delta^2} L = i\pi. \tag{4.6.8}$$

Therefore,

$$(\kappa_{ac}^2 - \delta^2)L = -\pi^2, \tag{4.6.9}$$

which, after rearranging, becomes

$$\delta = \frac{1}{L}\sqrt{\kappa_{ac}^2 L^2 + \pi^2}. \tag{4.6.10}$$

From Eq. (4.3.12), assuming $\kappa_{dc} = 0$ and $d\phi/dz = 0$ (no chirp in the grating), we get

$$\delta = \frac{\Delta\beta}{2}, \tag{4.6.11}$$

so that the detuning from the peak to the first zero is

$$\Delta\beta L = 2\sqrt{\kappa_{ac}^2 L^2 + \pi^2}. \tag{4.6.12}$$

For identical modes, $\mu = v$, using Eq. (4.3.4) we get,

$$\Delta\beta = \frac{4\pi n_{eff}(\lambda_B - \lambda)}{\lambda\lambda_B} \approx \frac{4\pi n_{eff}\Delta\lambda}{\lambda^2}, \tag{4.6.13}$$

where the bandwidth from the peak to the first zero is $\Delta\lambda$. Combining Eqs. (4.16.12) and (4.6.13), and noting that the bandwidth between the

first zeroes is twice the bandwidth between the peak and the first zero, leads to

$$2\Delta\lambda = \frac{\lambda^2}{\pi n_{eff} L}\sqrt{(\kappa_{ac}L)^2 + \pi^2}. \tag{4.6.14}$$

From Eq. (4.6.14) it follows that if $(\kappa_{ac}L)^2 \ll \pi^2$, then the bandwidth is an inverse function of the grating length as

$$2\Delta\lambda \approx \frac{\lambda^2}{n_{eff}L}, \tag{4.6.15}$$

while if the reverse is true, $(\kappa_{ac}L)^2 \gg \pi^2$, then the bandwidth is independent of the length of the grating and is proportional to the ac coupling constant,

$$2\Delta\lambda \approx \frac{\lambda^2\kappa_{ac}}{\pi n_{eff}}, \tag{4.6.16}$$

so that increasing κ_{ac} increases the bandwidth.

Zeroes in the reflection spectrum of the grating can be evaluated by using a similar analysis, to occur at

$$\alpha L = iM\pi, \qquad M = 1,2,3,\ldots \tag{4.6.17}$$

from which the corresponding detuning follows,

$$\Delta\lambda = \pm\frac{\lambda^2}{\pi n_{eff}}\sqrt{\kappa_{ac}\kappa_{ac}^* + \left(\frac{M\pi}{L}\right)^2}. \tag{4.6.18}$$

It is also useful to note the approximate position of the side-lobe peaks at

$$\alpha L = i\left(M + \frac{1}{2}\right)\pi, \qquad M = 1,2,3,\ldots, \tag{4.6.19}$$

which leads to

$$\delta\lambda_{sl} = \pm\frac{\lambda^2}{\pi n_{eff}}\sqrt{\kappa_{ac}\kappa_{ac}^* + \left[\frac{\left(M + \frac{1}{2}\right)\pi}{L}\right]^2}. \tag{4.6.20}$$

4.6.1 Phase and group delay of uniform period gratings

Figure 4.12 shows the phase response of the two gratings in Fig. 4.11, as a function of detuning, in units of radians per meter of grating. In the

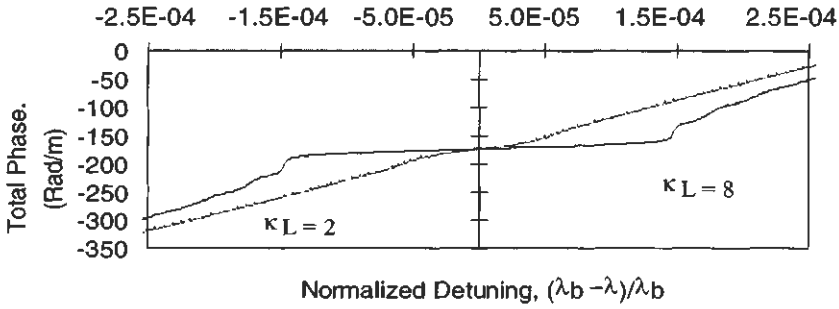

Figure 4.12: Total phase change in reflection from a uniform-period grating as a function of detuning for $\kappa_{ac}L = 2$ (dashed line) and $\kappa_{ac}L = 8$ (solid line). The stronger gratings behaves as a point reflector, since the phase change on reflection is large and almost constant for the same bandwidth when compared with the weaker grating.

region outside of the band stop of the grating, the phase of the light changes according to the unperturbed material refractive index. Into the band stop, the phase velocity slows down with increasing strength of the grating.

In Fig. 4.13 is the group delay of the same grating as in Fig. 4.12 in units of psec/m. This group delay per meter is

$$\frac{\tau}{L_g} = -\frac{1}{L_g}\frac{\lambda^2}{2\pi c}\frac{d\phi}{d\lambda}. \tag{4.6.21}$$

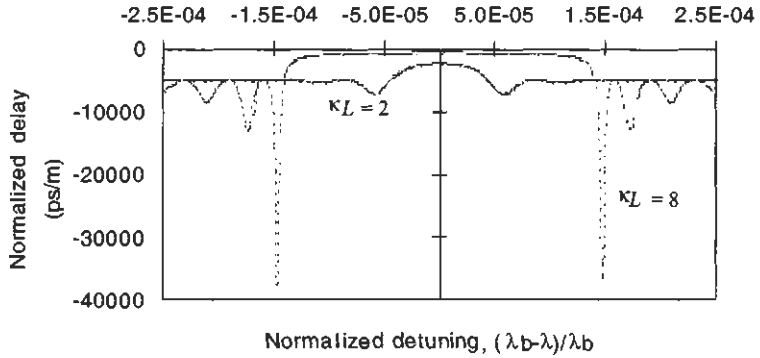

Figure 4.13: The normalized delay of a uniform period grating as a function of normalized de-tuning. For the larger coupling constant, the group delay in the center of the band is constant, while at the edges it increases rapidly, but is confined to a small spectrum.

Close to the edge of the band stop, strong dispersion can be seen with increasing strength of the grating. However, this dispersion is limited to a small bandwidth. At the center of the band, the group delay is a minimum and is approximately $1/(2\kappa_{ac}L_g)$ for gratings with a reflectivity close to 100%.

4.7 Radiation mode couplers

4.7.1 Counterpropagating radiation mode coupler: The side-tap grating

These gratings couple from a forward-propagating guided mode to a backward-propagating cladding mode, or a continuum of radiation modes. In this section, a new and simple theory is presented to gain a physical insight into the scattering of a guided mode into the counterpropagating radiation modes. The theory for radiation mode coupling has been presented elsewhere by various authors: Marcuse [2], Erdogan and Sipe [38], Mizrahi and Sipe [39], Erdogan [40], and Morey and Love [41]. These articles explain the phenomenon of radiation mode coupling using coupled mode theory and have successfully described the short-wavelength radiation loss from unblazed gratings [39], as well as the fine detailed spectrum observed under cladding mode resonance in tilted gratings [38,40]. Surprisingly little work has been reported on the application of these gratings. The term "side-tap" is appropriate for such gratings since the radiation is tapped from the side of the fiber, as happens when bending a fiber. A particular difference from bending is the reduced bandwidth and wavelength selectivity of the loss induced by such blazed gratings. Important properties of blazed gratings are their stability and low intrinsic temperature sensitivity, which may be reduced even further by appropriate design of fiber or coating [42,43]. Although the reflectivity into the counterpropagating guided mode is not generally zero, for acceptable performance in practical applications, it can be made very low by careful design of the filter.

The intention of this section is to provide a physical insight into the functioning of blazed gratings with the purpose of intentionally designing filters, which predominantly exhibit only radiation loss. The potential applications are numerous, e.g., in-fiber noninvasive taps, spectrum analyzers [44], and gain flattening of optical amplifiers using a single blazed grating [45] and multiple blazed gratings [46] and mode converters [47].

Figure 4.14 shows a schematic of the blazed "side-tap" grating written in the core of an optical fiber. The guided mode shown on the LHS of the figure can couple to the radiation field or to a "supermode" of a composite waveguide formed by the cladding and air interface. These are shown as a field distribution leaving the core at an angle and as a mode of the waveguide formed by the cladding, respectively. While the radiated fields form a continuum if unbounded [see Eq. (4.2.5)], they evolve into the bound supermodes of the composite waveguide in the presence of a cladding. The power in the radiated field and the radiated bound mode may grow provided the overlap of the interacting fields and the transverse distribution of the "source" (refractive index perturbation) is nonzero (see Section 4.2.3). The exchange of energy between the core mode and the radiated bound supermode is determined by the prevailing phase-matching conditions discussed in Section 4.2.5 and is solely a *coherent* interaction; the coupling to the unbound continuum of the radiation field is, however, only partly governed by this requirement. Physically, the radiated field exiting from the fiber core at a nonzero angle is spread away so that the distance over which it is coupled to the driving field is limited. This may be understood by the following: The driving mode field amplitude, which is assumed to be spatially constant, overlaps with a radiation field that is spreading

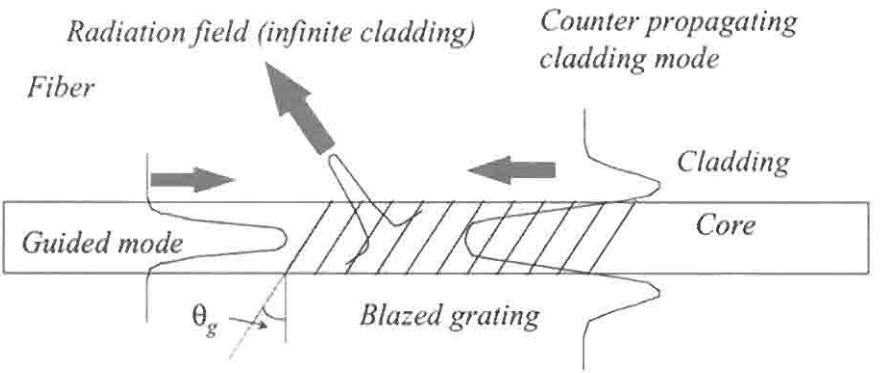

Bragg phase-matching condition:

$$2\pi n_{eff}/\lambda + 2\pi n_{cl}/\lambda = 2\pi N \cos\theta_g/\Lambda_g$$

Figure 4.14: Schematic of counter-propagating radiation field and bound cladding mode coupling from a forward propagating guided mode with a blazed grating.

rapidly away from the guided mode. For a coherent interaction, the fields must overlap over a distance with the correct phases. While the phases may remain synchronous, the radiated field spreads away, reducing the overlap as a function of propagation distance. With the cladding present, the field forms a mode, which propagates in the cladding and is then strongly coupled to the guided mode. This type of coupling is similar to simple Bragg reflection to discrete modes of the cladding. The transmission spectrum of a grating, which demonstrates this effect, is shown in Fig. 4.15. In this case, coupling is to modes of the HE_{1n} order (LP_{0n}), with a blaze angle close to zero. The cladding resonances are clearly visible.

Also shown in Fig. 4.14 is the equation describing the phase-matching condition for coupling to counterpropagating radiation at zero angles. This radiated field is at the *longest* wavelength at which coupling to the radiation field is possible, and only to zero-order modes, i.e., LP_{0m}. Note that the period of the grating, Λ_g, is dependent on the *sum* of the propagation constants of the guided driving mode and the radiated field (see also Fig. 4.5). As a consequence, any change in the cladding mode index only weakly affects the *radiated* field, but does change the coherent coupling to the supermodes. For a radiation mode tap, it is useful to consider the coupling to the unbounded radiation field. Another point to note is the angle of the *radiated* field, which is always slightly *more* than twice the tilt angle of the grating, apparent from Fig. 4.6. However, this angle is reduced when the overlap to the radiated field is taken into account.

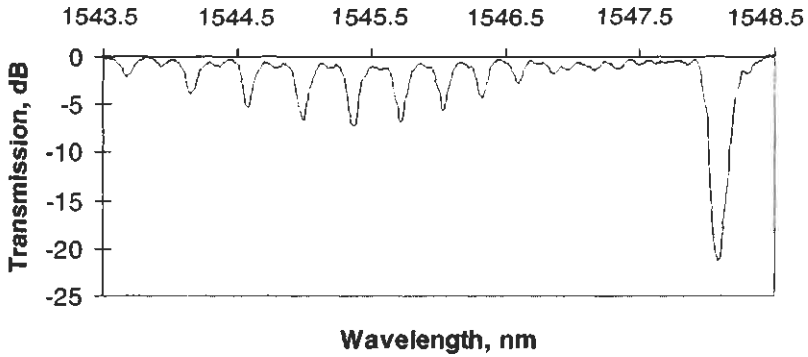

Figure 4.15: Cladding mode resonance in untilted gratings. On the right is the $LP_{01} \rightarrow LP_{01}$ guided mode reflection, while the others are to the LP_{0n} cladding modes (n = 2 to 10). See cover picture for example of cladding modes.

In Fig. 4.16 is shown the practical case of side illumination of optical fiber with UV irradiation. The absorption in the fiber causes the refractive index to be highly asymmetric [48]. This asymmetry is like a blaze, since one side of a propagating mode experiences more of a perturbation than the other. Consequently, such an asymmetric grating breaks the symmetry to allow coupling to odd, $l = 1$, order modes i.e., LP_{1m}. This is also true of blazed gratings, which are uniform across the core with the same effect on the guided mode.

A few points should be noted about scattering from a blazed grating. It is known that scattering of light from bulk blazed gratings [49] is directional and the phase-matching conditions easily derived for scattering, in thin and thick holograms [32]. The general approach taken in the next section is similar in so far as the scattering element is considered nonlocal and all the scattering events summed to arrive at the final unbounded coupling to the radiation field.

Theoretical model for coupling to the radiation field

The STG is a useful device for filter applications when used to couple the guided mode to the radiation field, rather than a mode. It forms a narrow band stop, whose spectral width is not dependent on the length of the grating in the same way as a Bragg grating. The wavelength and bandwidth is easily adjusted by choice of fiber, and the properties of the grating are as robust as those of the Bragg grating in terms of temperature

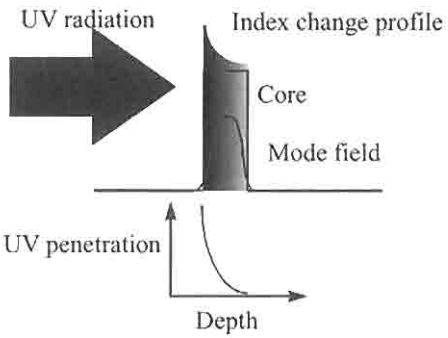

Figure 4.16: Effect of side illumination of a fiber core with UV radiation, giving rise to a tilted grating

sensitivity and strain. This allows the design of filters that depend only on the properties of the guidance of the core.

The side-tap grating is modeled as a periodic collection of uniform inclined planes of perturbed refractive index across the core. The mode fields are defined by the wave-guiding parameters, but it is assumed for the grating that the boundary of the cladding is absent; i.e., the grating is written in an infinite medium, although it is itself confined to the core. A consequence of this approximation is that refraction at the core–cladding boundary may be ignored, but can be accounted for later, to form modes. The assumption allows the design of *filters* in the same way in which the Bragg grating can be modified. The physical phenomenon of scattering is treated as Fraunhofer diffraction, with the amplitude of the scattering obeying the laws of conservation of energy. Figure 4.17 shows the schematic of the blazed grating. The mathematical description that follows shows that this type of a grating is equivalent to an infinite sum of small gratings written perpendicular to the axis of the fiber, but has an azimuthal dependence that makes it possible to couple to a particular set of radiation modes. In other words, the z-dependence of the grating due to the inclination of the planes is translated into a transverse variation in refractive index modulation, with the result that it immediately connects with the idea of the mode overlap integral, while separating the

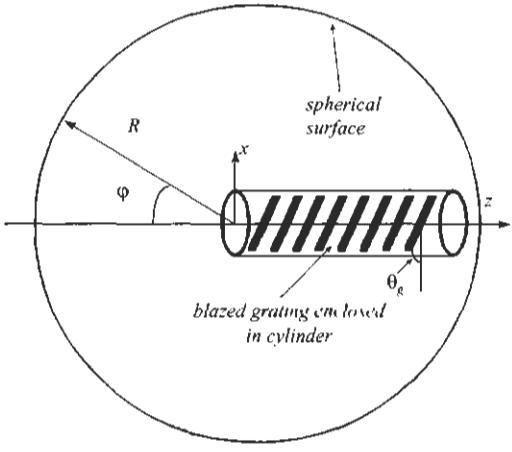

Figure 4.17: Scattering of power from a blazed grating entirely embedded in a cylinder.

issue of phase matching. The grating inclination angle is θ_g with respect to the transverse axis, x, in the x–z plane. The refractive index perturbation of the grating, $\delta n(x,y,x)$, simply described as a product of a grating of infinite extent and a "window" function W_{grating}, which takes account of the transverse variation in the amplitude of the grating, as

$$\delta n(x,y,z) = 2n\Delta n W_{grating}(r)\cos\left\{\left(\frac{2\pi N}{\Lambda_g}\right)(x\sin\theta_g - z\cos\theta_g)\right\}. \quad (4.7.1)$$

Converting Eq. (4.7.1) into cylindrical coordinates leads to the grating function

$$\delta n(r,\phi,z) = W_{grat}(r)2n\Delta n \times \left\{\begin{array}{l}\cos\left(\dfrac{2\pi Nz\cos\theta_g}{\Lambda_g}\right)\left(J_0(\gamma r) + 2\displaystyle\sum_{m=1}^{\infty}(-1)^m J_{2m}(\gamma r)\cos(2m\phi)\right) \\ + \sin\left(\dfrac{2\pi Nz\cos\theta_g}{\Lambda_g}\right)2\displaystyle\sum_{m=1}^{\infty}(-1)^m J_{2m+1}(\gamma r)\cos((2m+1)\phi)\end{array}\right\}, \quad (4.7.2)$$

where $\gamma = 2\pi N \sin\theta_g/\Lambda_g$. Equation (4.7.2) requires explanation, since it has real physical significance for the process of mode coupling. Each term on the RHS is responsible for coupling from the guided mode (here the fundamental) to a different set of radiation modes. Terms in the Bessel function J_m couple to modes with an azimuthal variation of $\cos(m\phi)$, i.e., to even-order radiation modes, while the J_0 terms leads to the guided mode back-reflection from the grating. Similarly, odd modes couple via the remaining set of terms within the curly brackets. Immediately obvious is the dependence of the back-reflection on γ, which periodically reduces the reflection to zero as a function of θ_g.

We refer to Fig. 4.17, in which a grating blazed at angle θ_g is shown entirely within a cylinder. The scattered total power at a wavelength λ impinging on a surface of radius R can be shown to be due to radiation from a current dipole situated at the grating [3] as

$$P_{scatter}(\lambda) = \int_{\phi=0}^{2\pi}\int_{\varphi=0}^{\pi} R^2 S_{scatter}(R,\phi,\varphi,\lambda)\sin\varphi\, d\varphi\, d\phi, \quad (4.7.3)$$

where ϕ is the angle between projection of the radius vector R and the x-axis. The Poynting vector is

$$S_{scatter}(R,\phi,\varphi,\lambda) = \frac{1}{2} n_{cl}\sqrt{\frac{\varepsilon_0}{\mu_0}}\,|E_{scatter}(R,\phi,\varphi,\lambda)|^2. \quad (4.7.4)$$

By integrating the scattered contributions from each part of the grating separated by δR, the scattered field, $E(R,\phi,\varphi,\lambda)$ may be derived by neglecting the angular dependence on φ and ϕ and follows as

$$E_{scatter}(R,\phi,\varphi,\lambda) = \frac{k^2 e^{i\beta_{clad}R}}{4\pi R} \iiint e^{i\beta_{clad}\delta R}\delta\varepsilon(x,y,z)E_{incident}(x,y,z)dxdydz. \tag{4.7.5}$$

The above result is consistent with Fraunhofer diffraction theory [3], and we note that it is in the same form as scattering due to the polarization response of a material. We note that far away from the grating,

$$\delta R \approx -x \cos\phi \sin\varphi - y \sin\phi \sin\varphi + z \cos\varphi. \tag{4.7.6}$$

The result in Eq. (4.7.5) neglects secondary scattering, so that it is implicitly assumed that the incident radiation is the primary cause for the radiation. This may be justified for STGs, since it is the aim of the exercise to consider radiation loss to the exclusion of reflection by proper choice of blaze angle, and because the radiation field is only weakly bound to the core.

We are now in a position to calculate the propagation loss of the incident radiation. The power scattered as a function of length of the grating described in Eq. (4.7.1) and into even azimuthal mode orders can be described as

$$P_{scatter}(z) = \alpha' P_{incident}(z)\cos^2(2\pi z \cos\theta_g/\Lambda_g)dz. \tag{4.7.7}$$

α' is a loss coefficient, which is dependent on the wavelength, the transverse profile of the grating, and the incident field and is equivalent to the overlap integral of Eq. (4.3.6). The incident field therefore decays as

$$P_{incident}(z) = P_{incident}(0) \times \exp\left[-\frac{\alpha' z}{2}\left\{1 + \frac{\Lambda_g}{4\pi z \cos\theta_g}\sin\left(\frac{4\pi z \cos\theta_g}{\Lambda_g}\right)\right\}\right]. \tag{4.7.8}$$

The contribution due to the oscillating term within the exponent becomes insignificant for large z, and the power decays as

$$P_{incident}(z) \approx P_{incident}(0)e^{-(\alpha' z/2)}. \tag{4.7.9}$$

From Eq. (4.7.9) follows the approximate decay of the incident electric field,

$$E_{incident}(x,y,z) \approx E_0(x,y)e^{(i\beta_f - \alpha)z}, \tag{4.7.10}$$

where $\alpha = \alpha'/4$ is a function of wavelength only, and β_f is the propagation constant for the incident fundamental mode. The longitudinal component of the guided mode field is small and has been neglected in Eq. (4.7.10).

The physical analogy of the STG as a distributed antenna is particularly useful, equivalent to an infinite sum of mirrors, each contributing to the light scattered from the fiber core. For small lengths, we have to include the oscillating term in quadrature in Eq. (4.7.8), but with $z \gg \Lambda_g$, the electric field for the fundamental mode decays approximately as it would for constant attenuation per unit length. The attenuation constant depends on wavelength and the transverse distribution of the grating and the incident field, but not on z. This approximate result suggests that the filter loss spectrum should be independent of the length of the grating, which is indeed the case.

To calculate the scattered power and the spectrum of the radiation, we use Eq. (4.7.6) in Eq. (4.7.5) and include the grating function $W_{grating}$ to arrive at

$$E_{scatter}(R,\phi,\varphi) = \frac{\Gamma}{R}\iint W_{grating}(x,y)E_0(x,y)e^{i\beta_{clad}(-x\cos\phi\sin\varphi - y\sin\phi\sin\varphi)} \times I_L(x,L_g)dxdy, \tag{4.7.11}$$

where L_g is the length of the fiber grating, the constant Γ is given

$$\Gamma = \frac{\beta_{clad}\Delta n e^{i\beta_{clad}R}}{\lambda}, \tag{4.7.12}$$

and $I_L(x, L_g)$ is obtained by integration with respect to z,

$$I_L(x,L_g) = \frac{e^{i\gamma x}}{2}\frac{e^{(i\Delta\beta_b-\alpha)L_g}-1}{i\Delta\beta_b-\alpha} + \frac{e^{-i\gamma x}}{2}\frac{e^{(i\gamma\beta_f-\alpha)L_g}-1}{i\Delta\beta_f-\alpha}, \tag{4.7.13}$$

where γ was defined in (4.7.2), and $\Delta\beta_f$ and $\Delta\beta_b$ are the forward and backward phase mismatch factors,

$$\begin{aligned}\Delta\beta_b &= \beta_f + \beta_{clad}\cos\varphi - \frac{2\pi\cos\theta_g}{\Lambda_g}\\ \Delta\beta_f &= \beta_f + \beta_{clad}\cos\varphi + \frac{2\pi\cos\theta_g}{\Lambda_g},\end{aligned} \tag{4.7.14}$$

where $\beta_{clad} = 2\pi n_{clad}/\lambda$, and the signs are consistent with the measurement of the angle, φ. The forward scattering process can easily be included

if necessary but is ignored for now. For the backward phase-matching condition, the radiation angle at resonance, φ_L, is given by the $\Delta\beta_f = 0$, as has been seen in Section 4.2.5, so that

$$\beta_f + \beta_{clad} \cos \varphi_L = 2\pi \cos \theta_g / \Lambda_g. \tag{4.7.15}$$

The last result is a longitudinal phase-matching condition, which is exactly the same as normal Bragg reflection. It requires that the path difference between light scattered from points that are both on a line parallel to the optical axis of the fiber, and on adjacent fringes of the grating, should be exactly λ (Fig. 4.18).

Ignoring the forward scatter, we find the scattered counterpropagating power from Eqs. (4.7.11), (4.7.3), and (4.7.4) as

$$P_{scatter}(\lambda) = \frac{1}{2} n_{clad} \sqrt{\frac{\varepsilon_0}{\mu_0}} \Gamma^* \Gamma e^{-\alpha L} \tag{4.7.16}$$

$$\times \int_{\phi=0}^{2\pi} \int_{\phi=0}^{\pi} |I_{core}(\gamma,\varphi,\phi)|^2 \frac{\sinh^2(\alpha L/2) + \sin^2(\Delta\beta_b L/2)}{\Delta\beta_b^2 + \alpha^2} \sin \varphi \, d\varphi \, d\phi,$$

where the overlap integral over the profile of the grating, which we refer to as the transverse phase-matching condition, is

$$I_{core}(\gamma,\varphi,\phi) \tag{4.7.17}$$

$$= \iint W_{grating}(x,y) E_0(x,y) e^{i[x(\gamma - \beta_{clad} \cos \phi \sin \varphi) - \beta_{clad} y \sin \phi \sin \varphi]} dx dy.$$

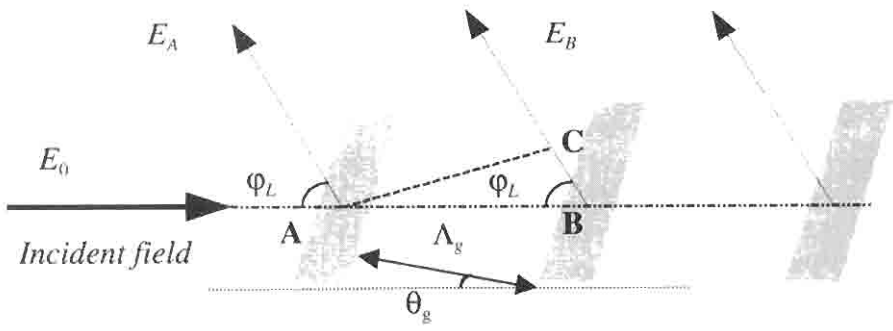

Figure 4.18: Scattered light from the fringe planes of the gratings adds up in phase when the resonance condition for longitudinal phase matching is met. AB + BC = $N\lambda$, at resonance.

In understanding the physics of the scattering, we consider separately the two components of the integral, the transverse phase-matching term (Eq. 4.7.17) and the longitudinal phase-matching (pm) term which depends on the detuning, $\Delta\beta_b$.

In the low-loss regime ($\alpha \ll \Delta\beta_b$), the longitudinal pm term is simply like the Bragg matched reflection condition, but now as a function of φ. For all practical purposes, this term is like a delta function that is only significant at very small angles of radiation ($\varphi \ll 1°$). The integral has a term dependent on $\cos\varphi$, which becomes broader and asymmetric in its angular bandwidth as $\varphi \to 0°$ and which is also inversely dependent on the length of the grating. For typical filter lengths of a few millimeters, we find the angular bandwidth to be ~1°. The asymmetry and broadening at small phase-matching angles have been observed in phase-matched second-harmonic generation with periodic structures [50].

In the high-loss regime, we find that the delta function broadens but has a width similar to that of the low-loss case. We can therefore choose to consider the dependence of the scattered power on the longitudinal phase matching as a very narrow filter at a given angle. Comparison of the longitudinal term with the transverse pm condition of Eq. (4.7.17) shows that the angular dependence of the radiation for the transverse case varies much more slowly and may be approximated to be a constant over the region of the longitudinal bandwidth. Figure 4.19 shows the dependence of the longitudinal and the transverse pm as a comparison for standard fiber and a uniform grating profile, $W_{grating} = 1$. The longitudinal response for a blaze angle of 5° and the transverse response for three blaze angles are shown.

The analytical result for the loss coefficient α has been shown to be [51],

$$\alpha \approx \frac{k^2 a^2 \beta_{clad} \Delta n^2}{32\pi^2} \frac{\int_{\phi=0}^{2\pi} |I_{core}(\gamma, \varphi, \phi)|^2 d\phi}{\int_{r=0}^{\infty} r E_0^2(r) dr}. \tag{4.7.18}$$

By normalizing the radius as $\rho = r/a$ (a is the core radius),

$$\alpha \approx \frac{\pi k^2 a^2 \beta_{clad} \Delta n^2}{4} \frac{I_0^2 + 2\sum_{m=1}^{\infty} I_m^2}{\int_{r=0}^{\infty} \rho E_0^2(\rho) d\rho}, \tag{4.7.19}$$

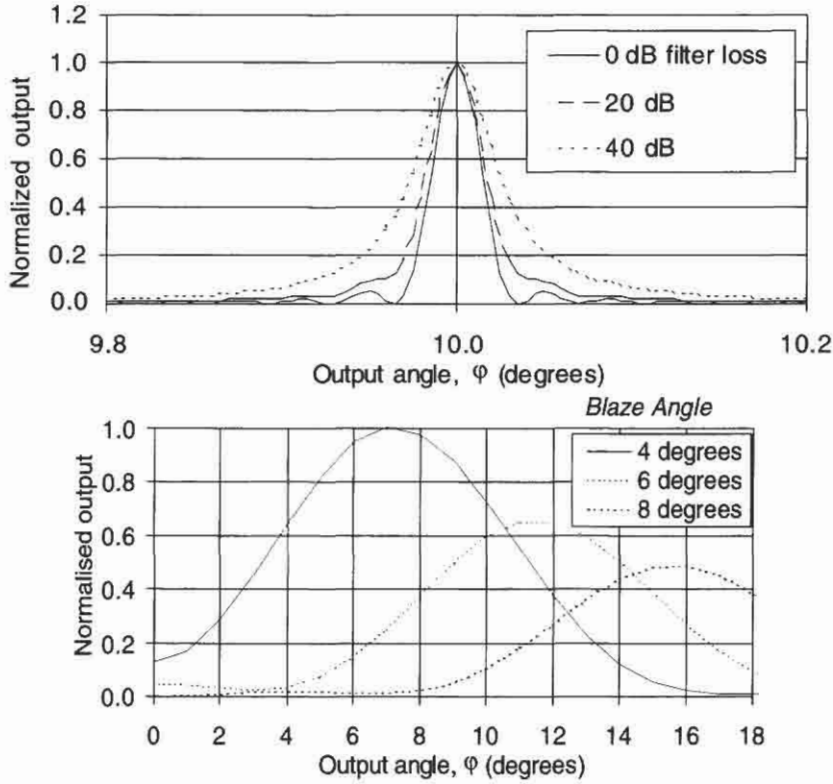

Figure 4.19: (a) shows the longitudinal integral and (b) is the transverse integral for different blaze angles.

and $E_0(\rho)$ is the field distribution of the fundamental mode. The integrals I_0 and I_m are defined as

$$I_0 = \int_{R=0}^{\infty} W_{grat}(\rho)E_0(\rho)J_0(\gamma\rho a)J_0(\xi_L\rho a)\rho d\rho$$
$$I_m = \int_{r=0}^{\infty} W_{grat}(\rho)E_0(\rho)J_m(\gamma\rho a)J_m(\xi_L\rho a)\rho d\rho. \tag{4.7.20}$$

In Eq. (4.7.20), we remind ourselves that γ is the transverse grating momentum that allows the mode to couple out of the core and is a function of the grating period as well as the blaze angle,

$$\gamma = \frac{2\pi \sin \theta_g}{\Lambda_g}. \tag{4.7.21}$$

ξ_L is the transverse momentum of the mode, depending on the output radiation angle of the scattered light, φ_L, at a given wavelength, and is

$$\xi_L = \beta_{clad} \sin \varphi_L. \tag{4.7.22}$$

In Fig. 4.20 is shown the calculated and measured loss spectrum of fibers with nominally the same v-value, but different core radii. The agreement between the measured loss and the calculated loss spectrum is quite good for two fibers. The blaze angle for the grating is 8°. The results also show that the loss spectrum due to scattering into the radiation modes is independent of the fiber length, and, indeed, this has been confirmed by experimental observations [51].

The reflection coupling constant for a tilted grating [38] with an arbitrary profile is

$$\kappa_{ac} \propto \frac{\int_{\rho=0}^{\infty} \rho W_{grating}(\rho) J_0(2\pi a \sin \theta_g \rho/\Lambda) E_0^2(\rho) d\rho}{\int_{\rho=0}^{\infty} \rho E_0^2(\rho) d\rho}. \tag{4.7.23}$$

This integral has been plotted in Fig. 4.21 and shows that zero Bragg reflection into the guided mode occurs at a lower blaze angle if the grating is moved outward from the core. For comparison, the back reflection from two fibers has been shown, one with a grating situated entirely in the cladding and the other with a standard telecommunications fiber core.

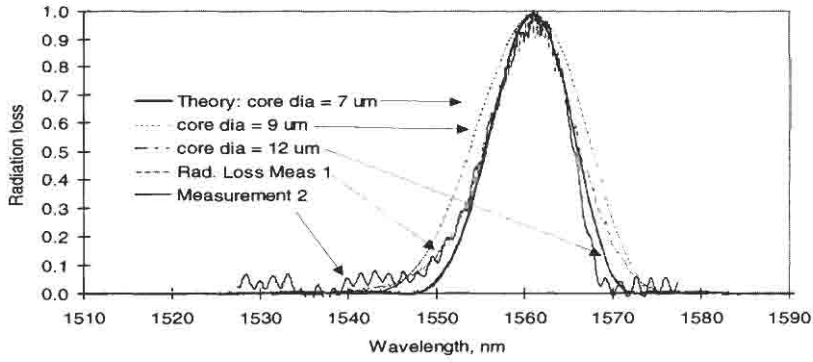

Figure 4.20: Measured radiation loss from large core weakly guiding fibers with radii of 7, 9, and 12 microns and a v-value of 1.9. Two measurements on 12-micron core-diameter fibers are also shown (after Ref. [52]).

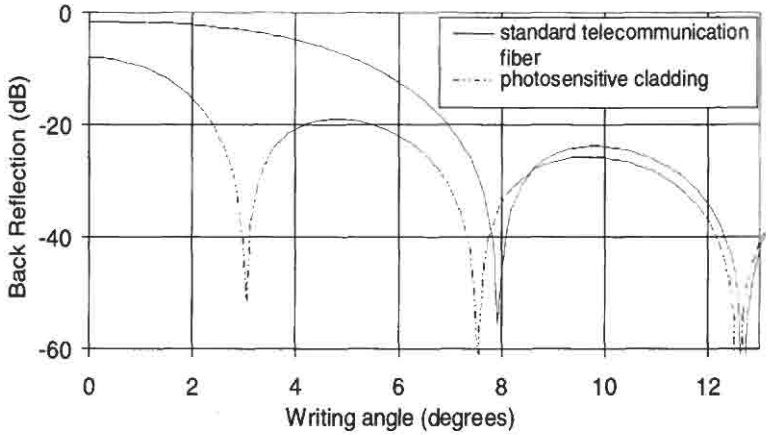

Figure 4.21: Comparison of back reflection from two fibers: both have nominally the same v-values, but one has a photosensitive cladding only (after Ref. [52]).

We note that the first back reflection minimum occurs at ~3° external writing angle for the photosensitive cladding fiber, compared with 8° for the standard fiber. This has an additional benefit of reducing the bandwidth over which radiation loss occurs, as seen from the phase-matching diagram in Section 4.2.5.

In Fig. 4.22 is shown the filter response for coupling to radiation modes for the photosensitive cladding fiber. The benefit of making the cladding photosensitive is clear, since it reduces the bandwidth at the zero reflection writing angle (measured at 3° and calculated for the fiber to be ~3.6°). The core radius of this fiber is 3.4 μm, and the photosensitive cladding extends from a to $4a$.

The agreement between the theoretical and experimentally observed properties of tilted fiber Bragg gratings is extremely good [38] using the complete theory presented by Erdogan [40,38]. In particular, the measured peak visible at 1545 nm in Fig. 4.22 is shown to be due to leaky mode coupling. The polarization dependence of tilted Bragg gratings in fibers with a core radius of ~2.6 μm and a core-to-cladding refractive index difference of 5.5×10^{-3} becomes obvious as the tilt angle exceeds 6.5° [38]. Above this angle, the p-polarization scatters less efficiently than the s-polarization. Below a tilt angle of 6.5°, the radiation loss is predominantly due to coupling to even-azimuthal order radiation modes, giving

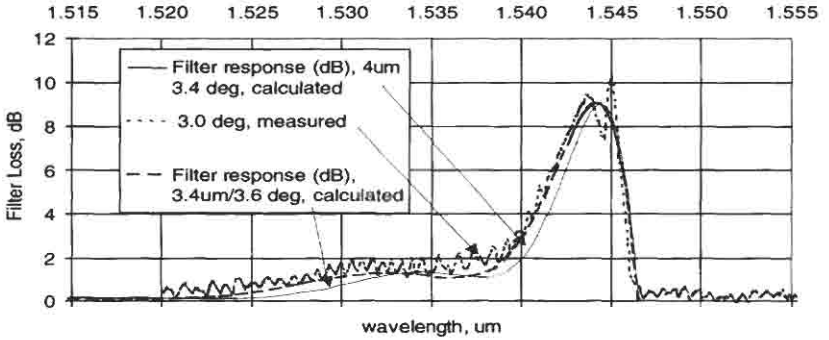

Figure 4.22: The loss spectrum (calculated and measured) for a photosensitive cladding fiber. The ripple in the loss spectra is a measurement artifact (after Ref. [52]).

rise to a sharp narrow-bandwidth peak. Above 6.5°, the coupling is to odd-azimuthal order modes and becomes much broader. By making angles for the back-reflection small (Fig. 4.21), one benefits from both low polarization sensitivity and a narrow-loss spectrum.

In Fig. 4.23 is shown the design diagram for STG filters as a function of the core-to-cladding refractive index difference, assuming an infinite

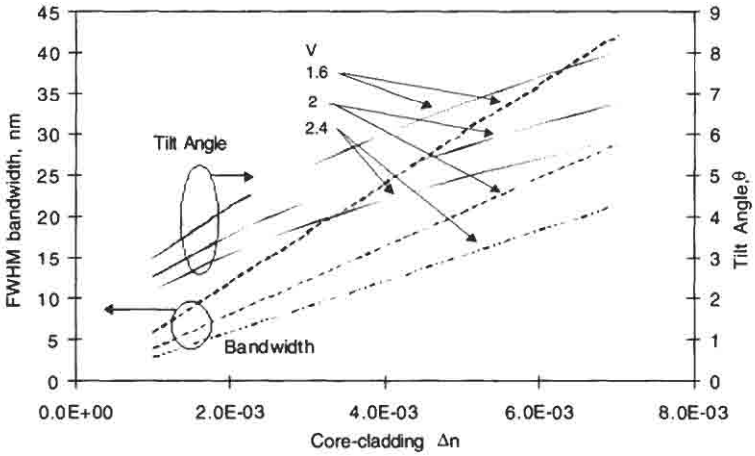

Figure 4.23: The design diagram for tilted STG filters with infinite cladding.

cladding. Two important parameters, the FWHM bandwidth and the tilt angle for zero back reflection into the fundamental mode for step index fibers for different v-values, are shown. The trend is as follows. Small core-cladding index difference and large v-value give the smallest radiation loss bandwidths, as well as the smallest tilt angles and accordingly the lowest polarization sensitivity. The penalty is the increased bend loss sensitivity.

4.7.2 Copropagating radiation mode coupling: Long-period gratings

These gratings couple light from forward-propagating guided modes to the forward-propagating cladding modes (as with an LPG) and the radiation field.

A schematic of the interaction and the phase-matching condition for coupling to forward-propagating radiation modes is shown in Fig. 4.24. The mode-coupling equations for forward coupling are given in Section 4.4 [Eqs. (4.4.11) and (4.4.12)]. The overlap integrals governing the interaction are shown in Eqs. (4.4.14)–(4.4.17) with the appropriate phase-matching terms. This type of coupling is similar to counterpropagating interactions, so far as the overlap of the modes is concerned. However, the power is exchanged between the radiated and guided modes periodically, as shown in Fig. 4.9, so that the filter length governs the bandwidth

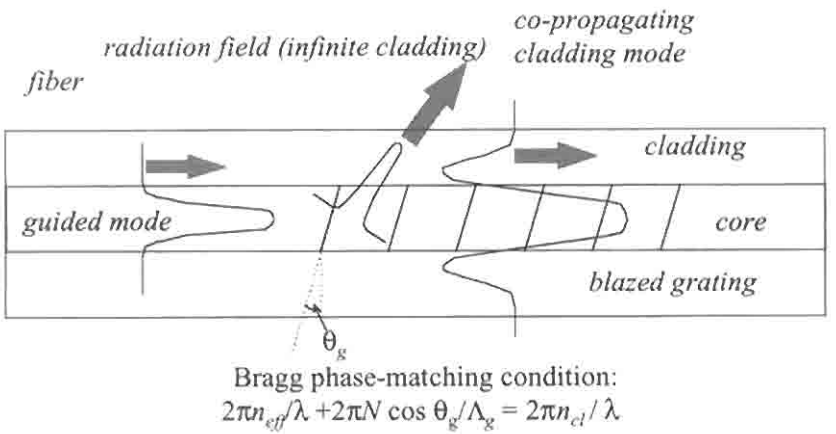

Figure 4.24: Schematic of co-propagating radiation field and bound cladding mode coupling from a forward propagating guided mode with a blazed grating.

of the coupling to the radiation mode (as it does to the individual cladding modes in the counterpropagating direction). The fundamental, LP_{01} guided mode can only couple to the even-order cladding modes of the same order, LP_{0n} [53]. Only if there is an asymmetry in the transverse profile will modes of different order couple. For example, in depressed cladding fibers that support a leaky LP_{11} mode, coupling to the LP_{16} mode is possible because of the very large overlap of the fields in the core [53], almost as large as the $LP_{01} \rightarrow LP_{01}$ modes. For fibers that support only the LP_{01} mode, a tilt in the grating allows coupling to copropagating (and counterpropagating) modes of different order. Erdogan has shown that the coupling constants to the radiation modes of the order v and the core mode (LP_{01}) follow the definitions of Eqs. (4.4.3) and (4.4.4). They are [40]

$$\kappa_{v\rightarrow 01}(z) = \frac{n\omega\varepsilon_0\Delta n(z)}{2}\int_0^{2\pi} d\phi \int_0^a (E_r^{clad}E_r^{core^*} + E_\phi^{clad}E_\phi^{core^*})rdr. \tag{4.7.24}$$

The eigenvalues and the field distributions for the cladding modes may be calculated by field matching at the boundaries as for the core for the low-order LP_{0n} modes, using a procedure similar to the guided core modes of the fiber [54]. Only coupling to the radiation modes with the azimuthal order $l = 1$ ($LP_{l-1,v}$ type) has a nonzero integral. The equations that describe the overlap integral, Eq. (4.7.24) of the modes for a transversely uniform grating are involved and cumbersome [40]. For the $v = 2, 4$ modes, the field in the core is very low, and therefore contributes little to the coupling. However, the field for the odd-numbered v modes has high intensity and these fields dominate the coupling for the lower-order modes. In Fig. 4.25 is shown the calculated coupling constants for a set of 168 cladding modes for a fiber at 1550 nm, normalized to the refractive index modulation, $\Delta n(z)$. The important point is that coupling to the low-even-order modes is weak compared to the odd modes. For $v > 40$, both even and odd order modes have almost identical coupling constants, but remain <20% of the maximum possible for the odd modes. Therefore, for many applications, it is necessary only to take account of a maximum of first 20–30 cladding modes, especially when computing the loss spectrum of an infinite cladding fiber (pure radiation loss).

A major difference between the STG and the LPG is shown in the phase-matching Eq. (4.7.14). We note that the detuning $\Delta\beta_f$ for a LPG is sensitive to the *difference* in the propagation constants of the guided and radiation modes. Any UV-induced change in the core index will result

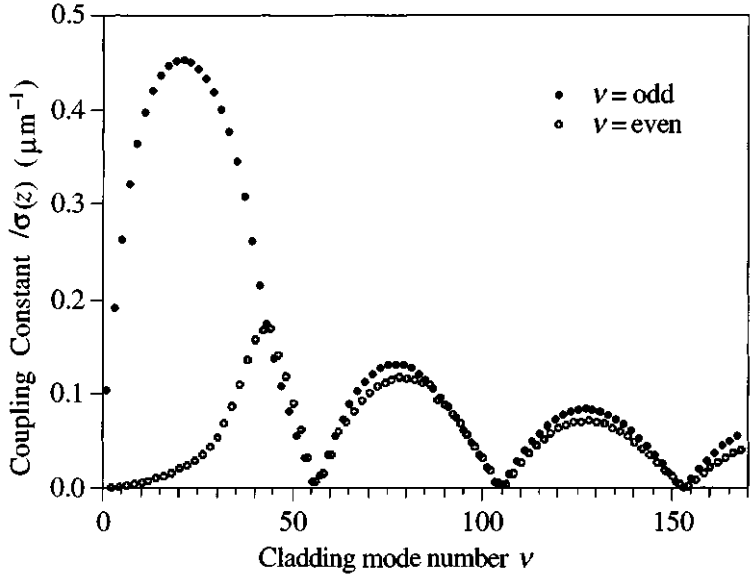

Figure 4.25: The coupling constants for the fundamental guided mode to 168 even- (l = 2) and odd-order cladding modes with azimuthal order 1 (type LP_{0n}) (from: Erdogan T, "Cladding mode resonances in short and long period fiber grating filters," *Opt. Soc. Am. A* ***14***(8), 1765, 1997.).

in a shift in the propagation constants, and thereby strongly affect the resonance wavelength. This aspect does not affect the counterpropagating resonance strongly, since the percentage change in the sum of the propagation constants is small. The change in the resonance condition for the STG in which only the core mode is affected can be calculated as [55]

$$\frac{\delta\lambda_{STG}}{\lambda_{STG}} = \frac{\eta\delta\beta_{UV}}{\beta_{core} + \beta_{clad}} \approx \frac{\eta\delta\beta_{UV}}{2\beta_0}, \tag{4.7.25}$$

whereas the resonance condition for the LPG changes as

$$\frac{\delta\lambda_{LPG}}{\lambda_{LPG}} = \frac{\eta\delta\beta_{UV}}{\beta_{core} - \beta_{clad}} \approx \frac{\eta\delta\beta_{UV}}{\Delta\beta}, \tag{4.7.26}$$

β_0 is the average propagation constant of the core and cladding modes, and $\eta\delta\beta_{UV}$ is the effect of the additional UV-induced detuning over and

above the initial mismatch, $\Delta\beta$ between the modes, and η is the overlap of the field within the core. A comparison between the two leads to

$$\delta\lambda_{LPG} \approx \frac{2n_{core}}{\delta n_{core \to clad}} \delta\lambda_{STG}. \tag{4.7.27}$$

In Eq. (4.7.27) the average effective index has been replaced by n_{core} and the difference in the mode propagation constants by the core-to-cladding index difference. Therefore, for a typical fiber, the LPG is between $\sim\times100$ and $\times1000$ more sensitive than the STG to the changes *between* the propagation constants of the core and the cladding modes.

The transmission spectra of a typical LPG is shown in Fig. 4.26. A number of resonances beginning with the coupling of the fundamental guided mode to the cladding n = 2, 3, 4, 5, and 6 modes can be seen. It should be noted that the transmission loss for each mode depends on the strength of the coupling constant κ_{ac} and κ_{dc}. The former indicates the length of the grating required for 100% coupling, while the latter causes the resonance wavelengths to shift [see Eq. (4.7.26)]. This requires a grating period to be adjusted according to the conversion efficiency *and*

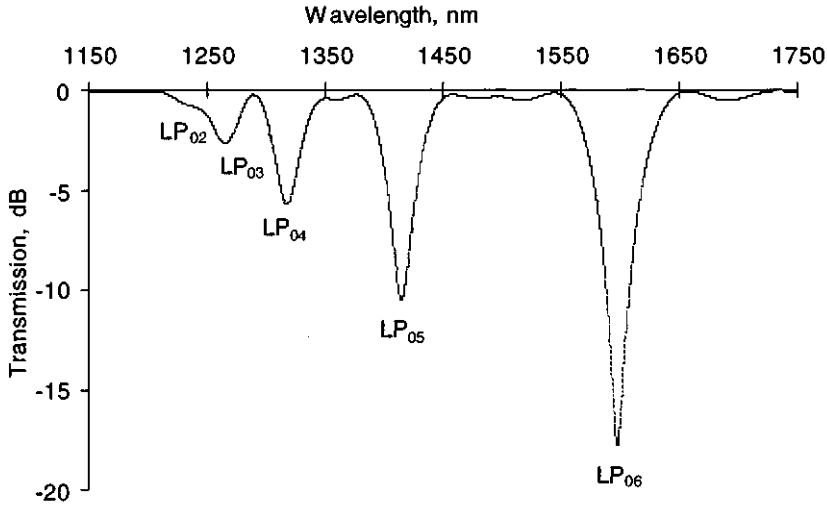

Figure 4.26: Transmission spectra of a ten mm long LPG in standard single mode type fiber (Corning SMF 28), with a period of 450 μm. Coupling is shown from the fundamental core mode to the odd (v = 1), n = 2 $\rightarrow$ 6 cladding modes (LP_{0n}).

the required resonance wavelength. The bandwidth of a single resonance of an LPG filter is approximately [56]

$$\Delta\lambda \approx \frac{\lambda_{resonance}^2}{\Delta n_{eff} L_g} \sqrt{\frac{4\kappa_{v\to 01}}{\pi} L_g}, \tag{4.7.28}$$

where coupling from the fundamental guided mode to the appropriate $1v$ cladding mode has the core-to-cladding mode effective index difference of Δn_{eff}. The resonance wavelength is determined by Eq. (4.6.4).

Long-period gratings for coupling a guided mode to the cladding may be designed for standard single-mode fibers by the data in Figs. 4.27 and 4.28. The period of a grating normalized to resonance wavelength $\lambda_{resonance}$ is shown as a function of the difference of guided mode effective index from the cladding index. For example, a resonance peak at 1550 nm requires a grating with a period $100 \times 1.55 = 155$ microns for a mode-effective index difference of 0.01.

We note that the change in the resonance wavelength of a long-period grating is influenced by the change in the core refractive index as a grating is being written [Eq. (4.7.30)]. As the coupling constant increases, the coupling loss increases until [Eq. (4.4.12)]

$$\alpha L_g = \frac{\pi}{2}, \tag{4.7.29}$$

and at the resonance wavelength, $\alpha = \kappa_{ac}$. To maintain the maximum loss, the length of the grating or the coupling constant has to be adjusted for a given bandwidth.

Figs. 4.27 and 4.28 may also be used to show how the period of the grating varies as a function of the *change* in the effective index of the mode. The desired resonance wavelength for an LPG may be calculated for the final mode effective index after the grating has been fabricated, using the data in Fig. 4.28 for the real modes of standard SMF fiber. For a required transmission loss, the refractive index modulation can be calculated to arrive at the final mode effective index. With this data, and from the required bandwidth of the grating, the appropriate choice for the grating period can be made.

Figure 4.29 shows the effect of immersing a long-period grating in oil. The resonance condition for coupling to the forward-propagating cladding mode is destroyed as the cladding is index matched. With further increases in the index of the oil, we note another resonance due to partial reflection

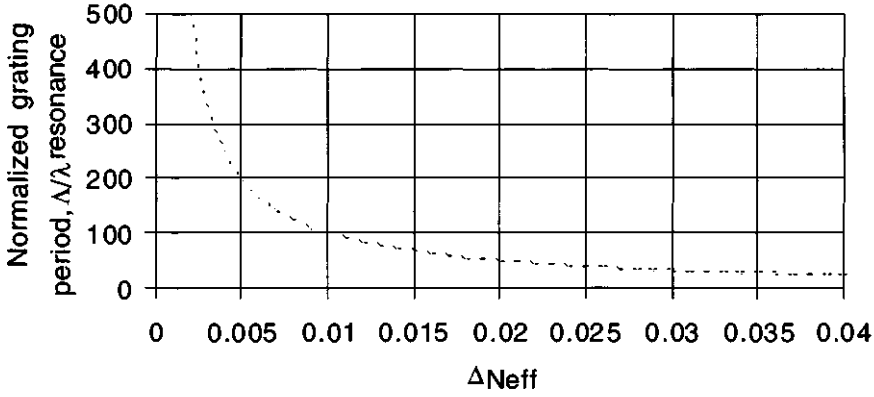

Figure 4.27: Normalized approximate resonance wavelength for phase-matched radiation mode coupling for LPG.

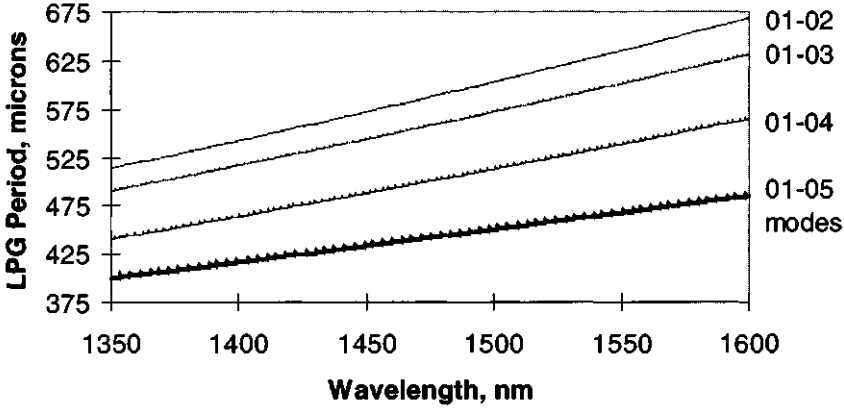

Figure 4.28: The computed grating periods for coupling of the LP_{01} core mode to the of the first four LP_{0n} cladding modes in standard (Corning SMF) fiber.

at the cladding surface to form leaky modes. The loss (to $1/e^2$ of the input) by leakage at the boundary of the cladding and the oil is [57]

$$L \approx -\left(1 + \frac{1}{\ln r}\right) L_b, \tag{4.7.30}$$

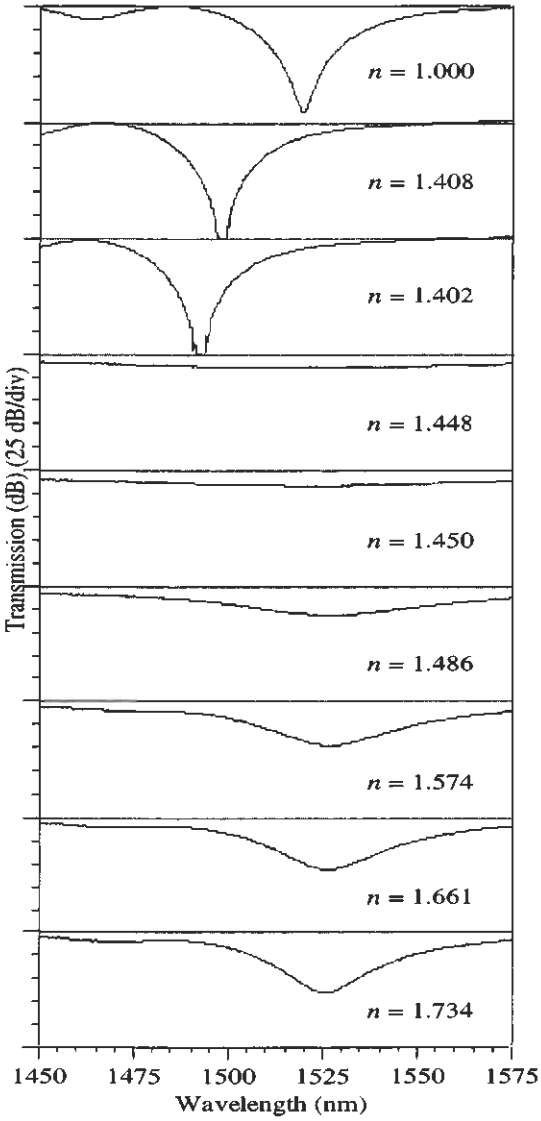

Figure 4.29: Radiation loss from a long-period grating as a function of the index of the oil that surrounds the fiber (from: Stegall D B and Erdogan T, "Long period fiber for grating devices based on leaky cladding modes," in *Bragg Gratings, Photosensitivity, and Poling in Glass Fibers and Waveguides: Applications and Fundamentals*, Vol. 17, OSA Technical Digest Series (Optical Society of America, Washington DC, 1997), paper BSuB2, pp. 16–18.).

where r is the Fresnel amplitude reflection coefficient at the cladding surface, and L_b is the distance between the successive reflections at the cladding surface.

4.8 Grating simulation

4.8.1 Methods for simulating gratings

Many of the techniques for simulating fiber Bragg gratings were introduced at the beginning of the chapter [10,58,9,19]. All the techniques have varying degrees of complexity. However, the simplest method is the straightforward numerical integration of the coupled-mode equations such as Eqs. (4.3.9) and (4.3.10). While this method is direct and capable of simulating the transfer function accurately, it is not the fastest. Another technique is based on the Gel'Fand–Levitan–Marchenko inverse scattering [58] method. This is again a powerful scheme based on integral coupled equations but has the primary disadvantage of obscuring the problem being solved. It has, however, the advantage of allowing a grating with particular characteristics to be designed. Perhaps the most attractive method is based on techniques developed for the analysis of metal waveguides by Rouard [11] and carries his name as a result. This technique, extended by Weller-Brophy and Hall [12], works on the principle that the waveguide may be segmented into subwavelength thin films. Standard thin-film techniques for calculating the amplitude and phase of the transmitted and reflected electric fields at each interface are propagated backward from the output end of the grating. The method is slow, but is one of the few that offers complete piecemeal control of the spatial variation in the refractive index modulation of the grating. For example, the transfer function of a grating with a sawtooth modulation is analyzed equally as well as a square or sinusoidal profile. The influence on the phase and amplitude response of the grating cannot be fully characterized if the Fourier coefficient of the phase-synchronous term for phase matching as shown in Eq. (4.2.27) alone is used. Thus, it is a laborious and time-intensive computation; however, the results accurately simulate the characteristics of complex-shaped grating periods with reasonable reflectivities, being limited by the rounding errors in the computation.

A fast and accurate technique is based on the T-matrix (transfer) for calculating the input and output fields for a short section δl of the grating

[10]. The outputs of the first matrix M^1 are used as the input fields to the second matrix, M^2, not necessarily identical to M^1. The process is continued until an entire complex profile grating is modeled. This method is capable of accurately simulating both strong and weak gratings, with or without chirp and apodization. It has the advantage of handling a *single* period of grating as the minimum unit length for the matrix in the case when the period or amplitude is a *slowly* varying function of length. In the following section, two methods, Rouard's and the T-matrix, will be presented for simulating gratings of arbitrary profile and chirp.

4.8.2 Transfer matrix method

An analytical solution for a grating of length L_g, with an arbitrary coupling constant $\kappa(z)$ and chirp $\Lambda(z)$, is desirable but no simple form exists. The variables cannot be separated since they collectively affect the transfer function. In the T-matrix method, the coupled mode equations [for example, Eq. (4.3.9)] are used to calculate the output fields of a short section δl_1 of grating for which the three parameters are assumed to be constant. Each may possess a unique and independent functional dependence on the spatial parameter z. For such a grating with an integral number of periods, the analytical solution results in the amplitude reflectivity, transmission, and phase. These quantities are then used as the input parameters for the adjacent section of grating of length δl_2 (not necessarily $= \delta l_1$). The input and output fields for a single grating section are shown in Fig. 4.30. The grating may be considered to be a four-port device with

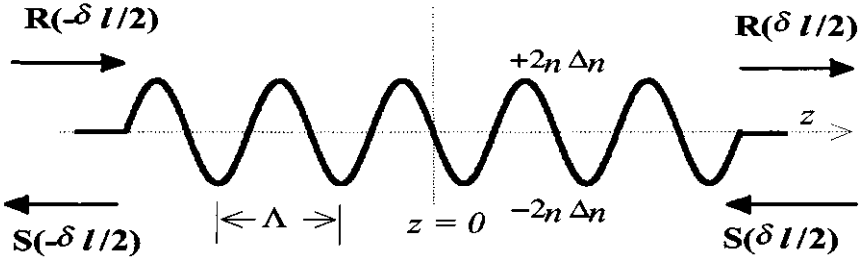

Figure 4.30: Refractive index modulation in the core of a fiber. Shown in this schematic are the fields at the start of the grating on the LHS and the fields at the output on the RHS. The modulated refractive index is $\pm$ $2n\Delta n$ about a mean index.

four fields: input fields $R(-\delta l_1/2)$ and $R(\delta l_1/2)$ and output fields $S(-\delta l_1/2)$ and $S(\delta l_1/2)$. A transfer matrix T^1 represents the grating amplitude and phase response. For a short uniform grating, the two fields on the RHS of the following equation are transformed by the matrix into the fields on the LHS as

$$\begin{bmatrix} R(-\delta l_1/2) \\ S(-\delta l_1/2) \end{bmatrix} = [T^1] \begin{bmatrix} R(\delta l_1/2) \\ S(\delta l_1/2) \end{bmatrix}. \tag{4.8.1}$$

The boundary conditions applied to Eq. (4.8.1) lead directly to the reflectivity and transmissivity of the grating. These conditions depend on whether the grating is a contradirectional or a codirectional coupler.

Reflection grating

For a reflection grating, the input field amplitude $R(-\delta l_1/2)$ is normalized to unity, and the reflected field amplitude at the output of the grating $S(\delta l_1/2)$ is zero, since there is no perturbation beyond the end of the grating.

Writing the matrix elements into Eq. (4.8.1) and applying the boundary conditions leads to

$$\begin{bmatrix} 1 \\ S(-\delta l_1/2) \end{bmatrix} = \begin{bmatrix} T_{11} & T_{12} \\ T_{21} & T_{22} \end{bmatrix} \begin{bmatrix} R(\delta l_1/2) \\ 0 \end{bmatrix}, \tag{4.8.2}$$

in which, the superscript for T^1 has been dropped for clarity. The transmitted amplitude is easily seen to be

$$R(\delta l_1/2) = \frac{1}{T_{11}}. \tag{4.8.3}$$

The reflected amplitude follows from Eqs. (4.8.2) and (4.8.3) as

$$S(-\delta l_1/2) = \frac{T_{21}}{T_{11}}. \tag{4.8.4}$$

Consequently, these are now the new fields on the RHS that can be transformed again by another matrix, T^2 and so on, so that for the entire grating after the Nth section, where $L = \sum_{j=1}^{N} \delta l_j$, is

$$\begin{bmatrix} R(-L/2) \\ S(-L/2) \end{bmatrix} = [T^N] \cdots [T^3][T^2][T^1] \begin{bmatrix} R(L/2) \\ S(L/2) \end{bmatrix}, \tag{4.8.5}$$

in which the field amplitudes on the RHS are the same as the those expressed in Eq. (4.8.1).

Replacing the N multiplied 2×2 matrices in Eq. (4.8.5) by a single 2×2 matrix, we get the transfer function of the whole grating,

$$\begin{bmatrix} R(-L/2) \\ S(-L/2) \end{bmatrix} = [\mathbf{T}] \begin{bmatrix} R(L/2) \\ S(L/2) \end{bmatrix}, \tag{4.8.6}$$

where the matrix $\mathbf{T}$ is

$$[\mathbf{T}] = \prod_{j=1}^{N} [T^j]. \tag{4.8.7}$$

Now the transmissivity τ of the whole grating follows from Eqs. (4.8.3) and (4.8.4),

$$\tau = (1 - \rho) = \frac{R(L/2)}{R(-L/2)} = \frac{1}{T_{11}}, \tag{4.8.8}$$

and reflectivity ρ,

$$\rho = \frac{S(-L/2)}{R(-L/2)} = \frac{T_{21}}{T_{11}}. \tag{4.8.9}$$

From the solution to the coupled-mode equations (4.3.9) and (4.3.10), the transfer matrix elements for the jth section are

$$T_{11} = \cosh(\alpha \delta l_j) - \frac{i\delta \sinh(\alpha \delta l_j)}{\alpha} \tag{4.8.10}$$

$$T_{22} = \cosh(\alpha \delta l_j) + \frac{i\delta \sinh(\alpha \delta l_j)}{\alpha} \tag{4.8.11}$$

$$T_{12} = -\frac{i\kappa_{ac} \sinh(\alpha \delta l_j)}{\alpha} \tag{4.8.12}$$

$$T_{21} = \frac{i\kappa_{ac} \sinh(\alpha \delta l_j)}{\alpha}. \tag{4.8.13}$$

A schematic of the sectioned gratings with the relevant parameters is shown in Fig. 4.31.

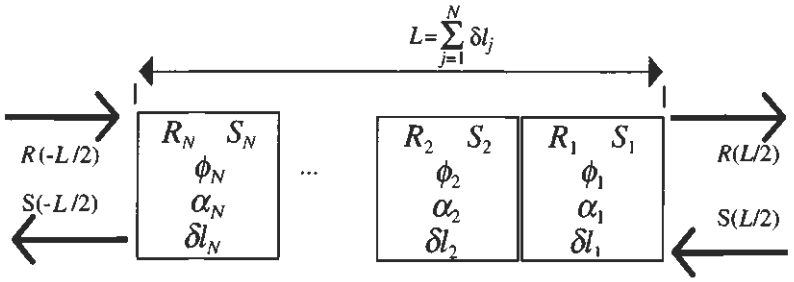

Figure 4.31: The concatenation of several short reflection gratings with constant parameters to form a composite grating. The phase ϕ_N is the phase of the grating in each section.

Codirectional coupling

For transmission gratings, different boundary conditions have to be used; $R(-L/2)$ is again normalized to unity. However, the field $S(L/2)$ on the LHS in Figure 4.30 is copropagating and has an amplitude of zero. At the output, $S(L/2)$ is also a copropagating mode. Codirectional coupling is shown in Figure 4.32. Applying boundary conditions, one arrives at

$$\begin{bmatrix}1\\0\end{bmatrix}=\begin{bmatrix}T_{11} & T_{12}\\ T_{21} & T_{22}\end{bmatrix}\begin{bmatrix}R(\delta l_1/2)\\ S(\delta l_1/2)\end{bmatrix}, \tag{4.8.14}$$

The uncoupled $[R(\delta l/2)]$ and cross-coupled $[S(\delta l/2)]$ amplitudes are then simply derived from Eq. (4.8.14) as

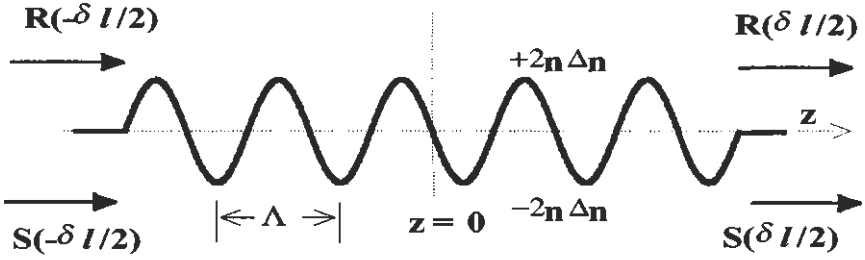

Figure 4.32: For codirectional coupling, the direction of propagation of the S-fields is reversed on both ends of the grating; compare with the reflection grating.

$$T_{11}R + T_{12}S = 1 \tag{4.8.15}$$
$$T_{21}R + T_{22}S = 0,$$

so that the crossed state amplitude is

$$S = \frac{1}{T_{12} - T_{11}(T_{22}/T_{21})}, \tag{4.8.16}$$

and the uncoupled amplitude,

$$R = \frac{T_{22}}{T_{21} - T_{11}T_{22}}. \tag{4.8.17}$$

Following the solutions for the codirectional coupled-mode Eqs. (4.4.9) and (4.4.10), the T-matrix elements for the jth section are

$$T_{11} = \cos(\alpha\delta l_j) + \frac{i\delta \sinh(\alpha\delta l_j)}{\alpha} \tag{4.8.18}$$

$$T_{22} = \cos(\alpha\delta l_j) - \frac{i\delta \sin(\alpha\delta l_j)}{\alpha} \tag{4.8.19}$$

$$T_{12} = \frac{i\kappa_{ac}\sin(\alpha\delta l_j)}{\alpha} \tag{4.8.20}$$

$$T_{21} = \frac{i\kappa_{ac}\sin(\alpha\delta l_j)}{\alpha}. \tag{4.8.21}$$

Equations (4.8.18–21) complete the analysis for guided-mode interactions.

Phase shifts within a grating

It is often useful and necessary to incorporate phase jumps within a distributed grating structure. The phase jump opens up a bandgap within the reflection bandwidth, creating a narrow transmission band. This procedure has been applied to distributed feedback (DFB) lasers to allow stable single-mode operation [59]. A phase shift is accomplished in the T-matrix by multiplying the reflectivity of the jth section by matrix elements containing only phase terms. On this basis, the transfer matrix takes on the form

$$\begin{bmatrix} R(-L/2) \\ S(-L/2) \end{bmatrix} = [T^N] \cdots [T^3][T_{ps}][T^1] \begin{bmatrix} R(L/2) \\ S(L/2) \end{bmatrix}, \tag{4.8.22}$$

where T_{ps} is the new phase-shift matrix for a reflection grating,

$$T_{ps} = \begin{bmatrix} e^{-i\phi/2} & 0 \\ 0 & e^{i\phi/2} \end{bmatrix}. \tag{4.8.23}$$

For codirectional coupling we replace the phase-shift matrix (4.8.23) by its conjugate. The phase factor, $\phi/2$, is any arbitrary phase and may be as a result of a change in the n_{eff} or a discontinuity within the grating. The phase change could have arisen from a region in which the grating was not present or from exposure to uniform UV radiation, thereby changing the local n_{eff}. In either case this phase

$$\phi = \frac{4\pi}{\lambda}(n_{eff} + \partial n)\Delta L, \tag{4.8.24}$$

where ∂n is the local phase change over a length ΔL. The calculation of the reflectivity and transmissivity proceeds in the same manner as without the phase step.

General conditions and restrictions for the T-matrix method

The transfer matrix method requires that certain conditions be met for accurate simulation of grating response [10]. First, when the grating parameters are a function of z, the minimum length of the section $\delta l_j \geq \Lambda_j \times K$, where K is a suitably large number. The actual factor K is a consequence of the slowly varying approximation. The magnitude of K depends on chirp rate $d\Delta\lambda/dL$ where $\Delta\lambda$ is the total chirp bandwidth in the grating. This value determines the upper limit to the number of sections allowed in any simulated grating. Figure 4.33 shows the effect on the reflectivity of reducing the number of sections from 37 periods to one period per section of a 2-mm-long grating with a chirp of 6 nm. The refractive index modulation is 2×10^{-3}.

Second, care must be taken to ensure that each section j has an integer number of grating periods in order to have a smooth transition between sections. An abrupt change in the grating modulation is equivalent to a phase jump and hence the formation of a Fabry–Perot cavity, as has been explained in Section 3.1.13. A consequence of not maintaining this condition over several sections is that it can lead to a deleterious effect outside of the bandwidth of the grating, by forming a superstructure of cascaded Fabry–Perot cavities.

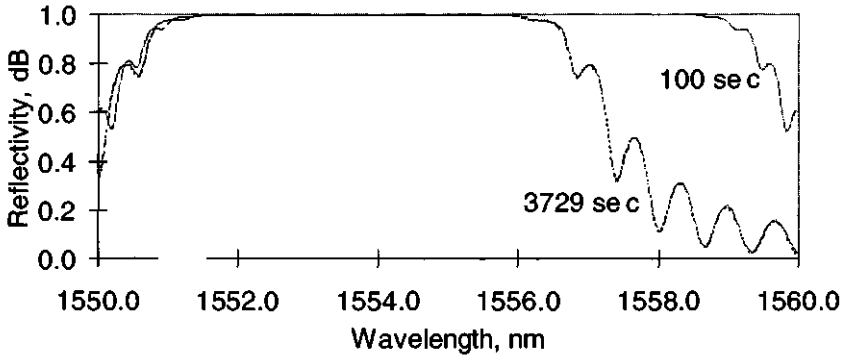

Figure 4.33: The effect of too many sections on the simulation of a 6-nm chirped 2-mm-long grating with 3729 (1 period/section) and 100 (37 periods/section) sections. The 100-section grating accurately models the grating, while the assumptions for the simulation are violated for too many sections.

Third, adequate care must also be taken to smooth any spatial variation in the refractive index modulation. Sections of constant κ_{ac} but different from adjacent ones inevitably form a superstructure [60, 61]. Superstructure can be responsible for replicas of the main Bragg reflection peak at far-removed wavelengths, causing spurious cross-channel interference in filters. The smaller the section, the wider the wavelength band over which the superstructure replicas may appear. Thus, there is a lower limit to the number of grating sections that must be used to reduce this detrimental effect. However, superstructure gratings, when carefully designed, can be used to perform useful functions [62] and are covered in Chapters 6 and 7.

Fourth, when simulating long chirped gratings, care must be taken to allow adequate spectral resolution in order to calculate the group delay accurately.

4.9 Multilayer analysis

4.9.1 Rouard's method

Simulation using this method relies on sectioning the grating into multilayers and replacing the layer by an interface with a complex reflectivity, which includes the phase change through the layer. To accurately

model the refractive index profile of the grating, the period may be subdivided into further sections. A recursive technique is then applied to calculate the reflectivity of the composite period of the grating. Thus, the problem is reduced to calculating the amplitude reflectivity ρ of each single period. The processes is repeated for N single-period sections, each with any local function for the refractive index modulation, period, or phase steps. It is easy to realize that any type of grating, microns or meters long, is then easily modeled. Alternatively, for certain types of pure sinusoidal refractive index modulation, the analytical solution for the constant period grating can be used [Eq. (4.3.11)] so long as the conditions described in Section 4.8.2 are adhered to. The power of this technique is, however, restricted by the computational errors when calculating the reflectivity and transmission of a large number of thin films. Despite this restriction, many types of gratings are adequately realized, provided the maximum reflectivity is limited to values ~99.99%. With care and appropriate computational algorithms, better results may be possible. The basic analysis is similar to the T-matrix approach; however, the reflectivity is simply calculated from the difference in the refractive index between two adjacent layers.

4.9.2 The multiple thin-film stack

Figure 4.34 shows a thin film on a substrate with light propagating at normal incidence and with transverse field components. The refractive index of each section is indicated. The reflectivities, r_1 and r_2, at each interface depends purely on the refractive indexes of the two dielectric materials on either side and are also shown.

The field in each region E_j is the sum of the forward R_j and backward, S_j, traveling fields:

$$E_j = R_j + S_j. \tag{4.9.1}$$

Applying continuity of the transverse field components (which are tangential to the interface) at the bottom layer, 1, and assuming propagation in a nonmagnetic medium, we get,

$$R_1 + S_1 = R_2 + S_2 \tag{4.9.2}$$

$$n_1(R_1 - S_1) = n_2(R_2 - S_2). \tag{4.9.3}$$

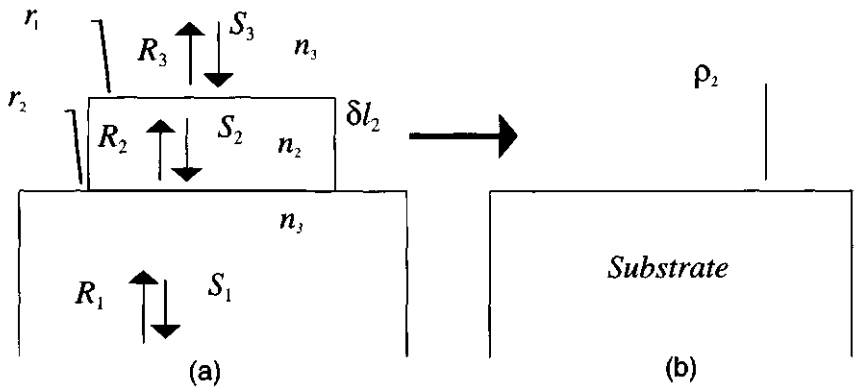

Figure 4.34: (*a*) Two layers on a substrate. The refractive index of each layer is also indicated. The left-hand figure is transformed into the problem shown in (*b*), with a complex reflectivity ρ_2 at the interface with the substrate, replacing the layer n_2.

Equations (4.9.2) and (4.9.3) can be expressed by algebraic manipulation in the following matrix form:

$$\begin{bmatrix} R_1 \\ S_1 \end{bmatrix} = \frac{1}{t_1} \begin{bmatrix} 1 & r_1 \\ r_1 & 1 \end{bmatrix} \begin{bmatrix} R_2 \\ S_2 \end{bmatrix}. \tag{4.9.4}$$

The reflectivity r_1 at the substrate interface is

$$r_1 = \frac{n_1 - n_2}{n_1 + n_2}, \tag{4.9.5}$$

and the transmission coefficient, t_1,

$$t_1 = \frac{2n_1}{n_1 + n_2}. \tag{4.9.6}$$

Once again applying continuity at the second interface from the bottom, the reflected and transmitted fields are described as

$$\begin{bmatrix} R_2 \\ S_2 \end{bmatrix} = \frac{1}{t_2} \begin{bmatrix} e^{i\varphi_2} & r_2 e^{i\varphi_2} \\ r_2 e^{-i\varphi_2} & e^{-i\varphi_2} \end{bmatrix} \begin{bmatrix} R_3 \\ S_3 \end{bmatrix}. \tag{4.9.7}$$

The phase $\varphi_j = \beta_j \delta l_j = 2\pi n_j \delta l_j / \lambda$.

As before for the matrix method, combining Eqs. (4.9.3)–(4.9.7) leads to

$$\begin{bmatrix} R_1 \\ S_1 \end{bmatrix} = \frac{1}{t_1 t_2} [T_1][T_2] \begin{bmatrix} R_3 \\ S_3 \end{bmatrix}. \tag{4.9.8}$$

Equation (4.9.8) may be simplified as for the T-matrix method as,

$$\begin{bmatrix} R_1 \\ S_1 \end{bmatrix} = [\mathbf{T}] \begin{bmatrix} R_3 \\ S_3 \end{bmatrix}, \tag{4.9.9}$$

from which the matrix elements follow as

$$\begin{aligned} T_{11} &= \frac{1}{t_1 t_2} (e^{i\varphi_2} + r_1 r_2 e^{-i\varphi_2}) \\ T_{12} &= \frac{1}{t_1 t_2} (r_2 e^{i\varphi_2} + r_1 e^{-i\varphi_2}) \\ T_{21} &= \frac{1}{t_1 t_2} (r_1 e^{i\varphi_2} + r_2 e^{-i\varphi_2}) \\ T_{22} &= \frac{1}{t_1 t_2} (r_1 r_2 e^{i\varphi_2} + e^{-i\varphi_2}). \end{aligned} \tag{4.9.10}$$

Applying the boundary condition in the region n_3, which is infinite, leads to $S_3 = 0$ as applied to Eq. (4.8.2). The simple complex reflectivity for the layer n_2 follows

$$\rho_2 = \frac{T_{21}}{T_{11}} = \frac{r_1 + r_2 e^{-i2\varphi_2}}{1 + r_1 r_2 e^{-i2\varphi_2}}, \tag{4.9.11}$$

and the transmission coefficient τ_2 is given by

$$\tau_2 = \frac{1}{T_{11}} = \frac{t_1 t_2}{e^{i\varphi_2} + r_1 r_2 e^{-i\varphi_2}}. \tag{4.9.12}$$

Replacing the second section by a single interface as shown in Fig. 4.34b and adding another layer with fields R_4 and S_4 above section 3, the composite reflectivity ρ follows from

$$\begin{bmatrix} R_1 \\ S_1 \end{bmatrix} = \frac{1}{\tau_2} \begin{bmatrix} e^{i\varphi_3} & \rho_2 e^{i\varphi_3} \\ \rho_2 e^{-i\varphi_3} & e^{-i\varphi_3} \end{bmatrix} \begin{bmatrix} R_4 \\ S_4 \end{bmatrix}, \tag{4.9.13}$$

so that in a similar manner to Eqs. (4.9.11) and (4.9.12),

$$\rho = \frac{T_{21}}{T_{11}} = \frac{r_4 + \rho_2 e^{-i2\varphi_3}}{1 + r_4 \rho_2 e^{-i2\varphi_3}}. \tag{4.9.14}$$

It is now straightforward to appreciate that a single period of a grating may be divided into j sections and the composite reflectivity computed using this piecewise linear method for any complex shape for the grating.

References

1. Gloge D., "Weakly guiding fibres," *Appl. Opt.* **10**(10), 2252–2258 (1971).
2. Marcuse D., in *Theory of Dielectric Optical Waveguides*. Academic Press, New York, 1994.
3. Snyder A. W. and Love J. D., in *Optical Waveguide Theory*. Chapman-Hall, London, 1983.
4. Kogelnik H. and Shank C. W., "Coupled wave theory of distributed feedback lasers," *J. Appl. Phys.* **43**, 2327–2335 (1972).
5. Kogelnik H., "Filter response of nonuniform almost-periodic structures," *Bell. Syst. Tech. J.*, **55**(1), 109–126 (1976).
6. Yariv A., in *Optical Electronics*, 4th ed. Saunders College Publishing (1991).
7. Hung-Chia H., in *Coupled Mode Theory*. VNU Science Express, The Netherlands (1984).
8. Haus H. A., in *Waves and Fields in Optoelectronics*. Prentice Hall, Englewood Cliffs, NJ, (1984).
9. Matsuhara M., Hill K. O., and Watanabe, "Optical waveguide filters: Synthesis," *J. Opt. Soc. Am.* **65**(7), 804–809 (1975).
10. Yamada M. and Sakuda K., "Analysis of almost periodic distributed feedback slab waveguides via a fundamental matrix approach," *Appl. Opts.* **26**(16), 3474–3478 (1987).
11. Rouard M. P., "Etudes des proprietes optiques des lames metalliques tres minces," *Annal. Phys. II* **7**(20), 1937.
12. Weller-Brophy L. A. and Hall D. G., "Analysis of waveguide gratings: application of Rouard's method," *J. Opt. Soc. Am. B* **2**(6), 863–871 (1985).
13. Weller-Brophy L. A. and Hall D. G., "Analysis of waveguide gratings: a comparison of the results of Rouard's method and coupled-mode theory," *J. Opt. Soc. Am. A* **4**(1), 60–65 (1987).

14. Elachi C., "Waves in active and passive periodic structures: a review," *Proc. IEEE* **64**, 1666–1698 (1976).
15. Russell P. St. J., "Bloch wave analysis of dispersion and pulse propagation in pure distributed feedback structures," *J. Mod. Opts.* **38**, 1599–1619 (1994).
16. Peral E. and Capmany J., "Generalized Bloch wave analysis for fiber Bragg and waveguide gratings," *J. Lightwave Technol.* **15**(8), 1295–1302 (1997).
17. Peral E., Capmany I., and Marti J., "Iterative solution to the Gel'Fand-Levitan Marchenko coupled equations and application to the synthesis of fibre gratings," *IEEE J. Quant. Electron.* **32**(12), 2078–2084 (1996).
18. Song G. H. and Shin S. Y., "Design of corrugated waveguide filters by the Gel'Fand-Levitan-Marchenko inverse scattering method," *J. Opt. Soc. Am.* **2**(11), 1905–1915 (1995).
19. Verly P. G., Dobrowolski J. A., Wild W. J., and Buron R. L., "Synthesis of high rejection filters with the Fourier transform method," *Appl. Opt.* **28**(14), 2864–2875 (1989).
20. Roman J. E. and Winnick K. A., "Design of corrugated waveguide filters by Fourier transform techniques," *IEEE J. Quantum. Electron.* **26**, 1918–1929 (1990).
21. Xia J., Jordan A. K. and Kong J. A., "Electromagnetic inverse-scattering theory for inhomogeneous dielectrics: the local reflection model," *J. Opt. Soc. Am.* **11**(3), 1081–1086 (1994).
22. Tikhonravov A. V. and Dobrowolski J. A., "Quasioptimal synthesis for antireflection coatings: a new method," *Appl. Opt.* **32**(22), 4265–4275 (1993).
23. Little B. E., Wu C. and Huang W. P., "Synthesis of codirectional couplers with ultralow sidelobes and minimum bandwidth," *Opt. Lett.* **20**, 1259 (1995).
24. Storoy H., Engan H. E., Sahlgren B., and Stubbe R. "Position weighting of Fiber Bragg gratings for bandpass filtering," *Opt. Lett.*, **22**(11), 784–786 (1997).
25. Winick K. A., "Effective-index method and coupled-mode theory for almost periodic waveguide gratings," *Appl. Opts.* **31**, 757–764 (1992).
26. Frolik J. L. and Yagle A. E., "An asymmetric discrete-time approach for the design and analysis of period waveguide gratings," *J. Lightwave. Technol.* **13**, 175–185 (1995).
27. Russell P. St. J. and Birks T. A., "A Hamiltonian approach to propagation in chirped and nonuniform Bragg grating structures," in *Proc. of OSA Topical meeting in Photosensitivity and Quadratic Nonlinearity in Glass Waveguides: Fundamentals and Applications*, Portland, OR, 1995, p. PMD2/257–260.
28. Poladin L., "Variational technique for nonuniform gratings and distributed feedback lasers," *J. Opt. Soc. Am.* **A-11**, 1846–1853 (1974).

29. Radic S., George N. and Agrawal G. P., "Analysis of nonuniform nonlinear distributed feedback structures: generalised transfer matrix approach," *IEEE J. Quantum Electron.* **31**(7), 1326–1336 (1995).

30. Matuschek N., Kärtner F. X., and Keller U., "Exact coupled mode theories for multilayer interference coatings with arbitrary strong index modulation," *IEEE J. Quantum Electron.* **33**(3), 295–302 (1997).

31. Johnson D. C., Bilodeau F., Malo B., Hill K. O., Wigley P. G. J. & Stegeman G. I., "Long length, long-period rocking filters fabricated from conventional monomode telecommunications optical fibres," *Opt. Lett.* **17**(22), 1635 (1992).

32. Kogelnik H., "Coupled wave theory for thick holograms," *Bell Syst. Tech. J.* **48**(9), 2909–2947 (1969).

33. Kreyszig E., in *Advanced Engineering Mathematics*, 5th Ed., p. 345. Wiley, New York (1992).

34. Stolen R. H., Ashkin A., Pliebel W., and Dziedzic, "In-line fiber polarization rocking rotator and filter," *Opts. Lett.* **9**, 300–303 (1984).

35. Hill K. O., Bilodeau F., Malo B., and Johnson D. C., "Birefringent photosensitivity in monomode optical fibre: application to external writing of rocking filters," *Electron. Lett.* **27**(1), 1548 (1991).

36. Russell P. St. J. and Hand D. P., "Rocking filter formation in photosensitive high birefringence optical fibres," *Electron. Lett.* **26**, 1846–1848 (1990).

37. Ouellette F., Gagnon D., and Porier M., "Permanent birefringence in Ge-doped fiber," *Appl. Phys. Lett.* **58**(17), 1813 (1991).

38. Erdogan T. and Sipe J. E., "Tilted fiber phase gratings," *J. Opt. Soc. Am. A* **13**, 296–313 (1996).

39. Mizrahi V. and Sipe J. E., "Optical properties of photosensitive fiber phase gratings," *J. Lightwave. Technol.* **11**, 1513–1517 (1996).

40. Erdogan T., "Cladding mode resonances in short and long period fiber grating filters," *J. Opt. Soc. Am. A* **14**(8), 1760–1773 (1997).

41. Morey W. W., Meltz G., Love J. D., and Hewlett S. J., "Mode-coupling characteristics of photo-induced Bragg gratings in depressed cladding fiber," *Electron. Lett.* **30**, 730–731 (1994).

42. Kashyap R., Hornung S., Reeve M. H., and Cassidy S. A., "Temperature desensitisation of delay in optical fibres for sensor applications," *Electron. Lett.* **19**(24), 1039–1040 (1983).

43. Kashyap R., Reeve M. H., Cassidy S. A., and Hornung S., "Temperature desensitization of delay in optical fibers". UK Patent no. *8328204*, March 31, 1987. US Patent no. *4923278*, May 8, 1990.

44. Wagener J. L., Strasser T. A., Pedrazzani J. R., and DeMarco J., "Fiber grating optical spectrum analyser tap," in *Tech. Digest of ECOC'97, Publn. No. 448*, pp. 65–68.

45. Kashyap R., Wyatt R., and Campbell R. J., "Wideband gain flattened erbium fiber amplifier using a blazed grating," *Electron. Lett.* **24**(2), 154–156 (1993).

46. Kashyap R., Wyatt R., and McKee P. F., "Wavelength flattened saturated erbium amplifier using multiple side-tap Bragg gratings," *Electron. Lett.* **29**(11), 1025 (1993).

47. Johlen D., Klose P., Renner H., and Brinkmeyer E., "Strong LP_{11} mode splitting in UV side written tilted fiber gratings," in *Bragg Gratings, Photosensitivity, and Poling in Glass Fibers and Waveguides: Applications and Fundamentals*, Vol. 17, OSA Technical Digest Series (Optical Society of America, Washington DC, 1997), paper BMG12, 219–221.

48. Lemaire P. J., Vengsarkar A. M., Reed W. A., and DiGiovanni D. J., "Thermal enhancement of UV photosensitivity in H_2 loaded optical fibers," in *Tech. Digest of Conf. on Opt. Fib. Commun., OFC'95*, paper WN1, pp.158–159.

49. See, for example, Syms R. A. and Cozens, in *Optical Guided Waves and Devices*, McGraw-Hill, London (1992).

50. Kashyap R., Figure 15, Inset in "Phase-matched periodic-electric-field-induced second-harmonic generation in optical fibres," *J. Opt. Soc. Am. B* **6**(3), 313–328 (1989).

51. Holmes M. J., Kashyap R., Wyatt R., and Smith R. R., "Ultra narrow-band optical fiber sidetap filter," *ECOC'98*, pp. 137–138, 1998.

52. Holmes M. J., Kashyap R., Wyatt R., and Smith R. P., "Development of radiation mode filters for WDM," in *Proc. of IEE Symposium on WDM Technology, IEE*, 16–17 June 1998.

53. Hewlett S. J., Love J. D., Meltz G., Bailey T. J., and Morey W. W., "Cladding-mode resonances in Bragg fibre gratings depressed and matched-cladding index profiles," in *Photosensitivity and Quadratic Nonlinearity in Glass Waveguides: Fundamentals and Applications*, Vol. 22, 1995 OSA Technical Series (Optical Society of America, Washington DC, 1995), pp. PMC2(235–238) (1995).

54. Monerie M., "Propagation in doubly clad single mode fibers," *IEE Trans. Microwave Theory and Techniques* **MTT-30**(4), 381–388 (1982).

55. Dianov E. M., Kurkov A. S., Medvedkov O. I., and Vasil'ev, "A new method for measuring induced refractive index change in optical fiber core," in *Photosensitivity and Quadratic Nonlinearity in Glass Waveguides: Fundamentals and Applications*, Vol. 22, 1995 OSA Technical Series (Optical Society of America, Washington DC, 1995), pp. SuB4-(104–107) (1995).

56. Hall D. G., "Theory of waveguides and devices," in *Integrated Optical Circuits and Components* L. D. Hutchinson, Ed. Marcel Dekker, New York (1987).

57. Stegall D. B. and Erdogan T., "Long period fiber grating devices based on leaky cladding modes," in *Bragg Gratings, Photosensitivity, and Poling in Glass Fibers and Waveguides: Applications and Fundamentals*, Vol. 17, OSA Technical Digest Series (Optical Society of America, Washington DC, 1997), paper BSuB2, pp. 16–18.

58. Roman J. E. and Winnick K. A., "Waveguide grating filters for dispersion compensation and pulse compression," *IEEE J. Quantum Electron.* **29**(3), 975 (1993).

59. Haus H. A. and Lai Y., "Theory of cascaded quarter wave shifted distributed feedback resonators," *IEEE J. Quantum Electron.* **28**(1), 205–213 (1992).

60. Jayaraman V., Cohen D. A., and Coldren L. A., "Demonstration of broadband tunability of a semiconductor laser using sampled gratings," *Appl. Phys. Lett.*, **60**(19), 2321–2323 (1992).

61. Ibsen M., Eggleton B. J., Sceats M. G., and Ouellette F., "Broadly tunable DBR fibre using sampled Bragg gratings," *Electron. Lett.* **31**(1), 37–38 (1995).

62. Ouellette F., Krug P. A., Stephens T., Doshi G., and Eggleton B., "Broadband and WDM dispersion compensation using chirped sampled fibre Bragg gratings," *Electron. Lett.* **31**(11), 899–901 (1995).

This page intentionally left blank